

Measurement of the neutron charge radius and the role of its constituents

H. Atac¹, M. Constantinou¹, Z.-E. Meziani^{2,1}, M. Paolone³, and N. Sparveris^{1,*}

¹Temple University, Philadelphia, PA 19122, USA

²Argonne National Laboratory, Lemont, IL 60439, USA

³New Mexico State University, Las Cruces, NM 88003, USA

*corresponding author, e-mail: sparveri@temple.edu

ABSTRACT

The neutron is a cornerstone in our depiction of the visible universe. Despite the neutron zero-net electric charge, the asymmetric distribution of the positively- (up) and negatively-charged (down) quarks, a result of the complex quark-gluon dynamics, lead to a negative value for its squared charge radius, $\langle r_n^2 \rangle$. The precise measurement of the neutron's charge radius thus emerges as an essential part of unraveling its structure. Here we report on a $\langle r_n^2 \rangle$ measurement, based on the extraction of the neutron electric form factor, G_E^n , at low four-momentum transfer squared (Q^2) by exploiting the long known connection between the $N \rightarrow \Delta$ quadrupole transitions and the neutron electric form factor. Our result, $\langle r_n^2 \rangle = -0.110 \pm 0.008$ (fm²), addresses long standing unresolved discrepancies in the $\langle r_n^2 \rangle$ determination. The dynamics of the strong nuclear force can be viewed through the precise picture of the neutron's constituent distributions that result into the non-zero $\langle r_n^2 \rangle$ value.

Introduction

The study of the nucleon charge radius has been historically instrumental towards the understanding of the nucleon structure. In the neutron case, it is the highly complicated dynamics of the strong force between quarks and gluons, the fermionic nature of quarks and spin-orbit correlations that leads to an asymmetric distribution of u- and d-quarks in it, thus resulting in a negative value for $\langle r_n^2 \rangle$. The precise measurement of $\langle r_n^2 \rangle$ becomes a critical part of our understanding of the nucleon dynamics. Furthermore, employing new, different techniques in extracting this fundamental quantity has proven most valuable, as recently exhibited in the proton's case: the disagreement of the proton charge radius, r_p , as determined using the Lamb shift measurement in the muonic hydrogen atom¹, with the earlier results based on the hydrogen atom and the electron scattering measurement, gave rise to the proton radius puzzle². In turn, this led to a significant reassessment of the methods and analyses utilized in the proton radius extraction, and to the consideration of physics beyond the standard model as potential solutions to this discrepancy. Various atomic and nuclear physics techniques were employed for the proton r_p measurement. However, in the neutron case, the determination of $\langle r_n^2 \rangle$ is more challenging since no atomic method is possible and the electron scattering method suffers from severe limitations due to the absence of a free neutron target. Thus, the extraction of $\langle r_n^2 \rangle$ has been uniquely based on the measurement of the neutron-electron scattering length b_{ne} , where low-energy neutrons are scattered by electrons bound in diamagnetic atoms.

The $\langle r_n^2 \rangle$ measurements adopted by the particle data group (PDG)³⁻⁶ exhibit discrepancies, with the values ranging from $\langle r_n^2 \rangle = -0.114 \pm 0.003$ ⁴ to $\langle r_n^2 \rangle = -0.134 \pm 0.009$ (fm²)⁵. Among the plausible explanations that have been suggested for this, one can find the effect of resonance corrections and of the electric polarizability, as discussed e.g. in Ref.⁴. However, these discrepancies have not been fully resolved, a direct indication of the limitations of this method.

An alternative way to determine $\langle r_n^2 \rangle$ is offered by measuring the slope of the neutron electric form factor, G_E^n , at $Q^2 \rightarrow 0$, which is proportional to $\langle r_n^2 \rangle$. In the past, determinations of G_E^n at finite Q^2 were typically carried out by measuring double polarization observables in quasi-elastic electron scattering from polarized deuterium or ³He targets using polarized electron beams⁷⁻²¹. However, these measurements were not able to access G_E^n at a sufficiently low Q^2 range so that the slope, and subsequently the $\langle r_n^2 \rangle$ can be determined.

In this work we rely on an alternative path to access G_E^n . It has long been known^{22,23} that the ratios of the quadrupole to the magnetic dipole transition form factors (TFFs) of the proton, $C2/M1$ (CMR) and $E2/M1$ (EMR), are related to the neutron elastic form factors ratio G_E^n/G_M^n . Here, we follow that path and we access G_E^n at low momentum transfers from high precision measurements of the two quadrupole TFFs. The main steps of this work are summarized here for clarity. First, we extract G_E^n from the quadrupole TFF data, at low momentum transfers²⁴⁻²⁸, utilizing the form factor relations^{22,23} determined within the SU(6) and the large- N_c frameworks. The variance of the G_E^n results from

the two analyses is treated as a theoretical uncertainty. The $G_E^n(Q^2)$ form factor is then parametrized and fitted to the data, and $\langle r_n^2 \rangle$ is determined from the G_E^n -slope at $Q^2 = 0$. Finally, we perform the flavor decomposition of the neutron and the proton form factors measurements and derive the flavor dependent quark densities in the nucleon, which reveal with high precision the role of the quark contributions to the neutron charge radius.

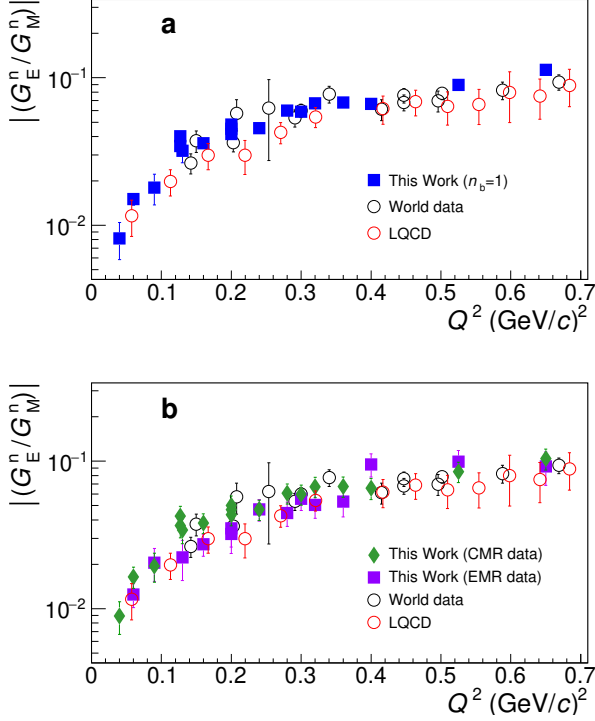


Figure 1. The elastic neutron form factor ratio.
a) The neutron electric to magnetic form factor ratio G_E^n/G_M^n : world data^{7–21} (black open circles), ratios calculated from the $N \rightarrow \Delta$ measurements^{24–32} through Eq. 1 for $n_b = 1$ (filled-squares), and lattice Quantum Chromodynamics (LQCD) results (red open circles)³³.
b) The G_E^n/G_M^n results from the large- N_c analysis of the Coulomb quadrupole measurements (CMR, filled diamonds) and of the Electric quadrupole measurements (EMR, filled boxes) from the experiments^{24–32}. The neutron world data (black open circles) and the LQCD results (red open circles)³³ are the same as in panel (a). The error bars correspond to the total uncertainty, at the 1σ or 68% confidence level.

Results

A consequence of the SU(6) spin and flavor symmetry group which relates the nucleon and the Δ resonance leads to the

following expression²²

$$\frac{G_E^n(Q^2)}{G_M^n(Q^2)} = \frac{Q}{|\mathbf{q}|} \frac{2Q}{M_N} \frac{1}{n_b(Q^2)} \frac{C2}{M1}(Q^2) \quad (1)$$

where $|\mathbf{q}|$ is the virtual photon three-momentum transfer magnitude in the γN center of mass frame and M_N is the nucleon mass. The n_b parametrizes the contribution from three-quark current terms, that tend to slightly increase the $C2/M1$ ratio (or correspondingly decrease the G_E^n/G_M^n), an SU(6) symmetry breaking correction that has been theoretically quantified to $\sim 10\%$ ²² (i.e. $n_b \sim 1.1$). If one chooses to follow the most conservative path, a theoretical uncertainty can be assigned to this term that is equal to the full magnitude of the symmetry breaking contributions i.e. $n_b = 1.1 \pm 0.1$. Considering the confidence with which the underlying theory is able to determine the level of the symmetry breaking contributions, the above assumption leads to a safe estimation, and most likely to an overestimation, of the theoretical uncertainty.

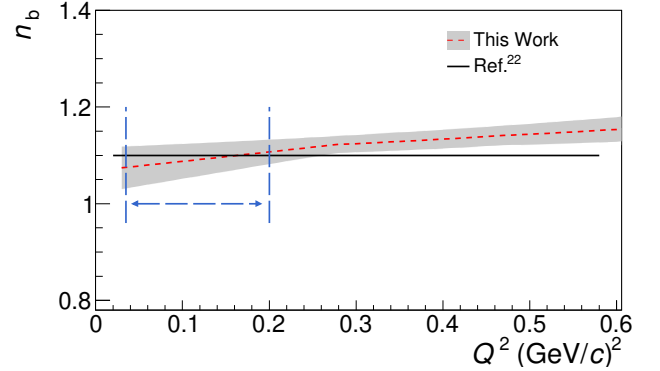


Figure 2. The experimentally determined symmetry breaking contributions.

The breaking corrections n_b (dashed line) and the associated uncertainty δn_b (shaded band) at the 1σ or 68% confidence level. The solid line indicates the n_b as theoretically determined in²². The horizontal double-arrow marks the Q^2 -range where the corrections have been employed for the measurement of G_E^n in this work.

In one of the first steps of this work we check the validity of the underlying theory using experimental measurements. The wealth of the TFF^{24–32} and of the G_E^n/G_M^n ^{7–21} world data allow to quantify the magnitude of the symmetry breaking corrections from the analysis of the experimental measurements. In Fig. 1a we show the neutron G_E^n/G_M^n world data^{7–14, 16–21} (open black circles), and we compare it to the G_E^n/G_M^n ratios that we have derived from the TFFs $C2/M1$ measurements^{24–32} (filled boxes) utilizing Eq. 1 with $n_b = 1$ (i.e. uncorrected for the symmetry breaking contributions). By parametrizing the two data sets and then forming their ratio we can experimentally determine the magnitude of the $n_b(Q^2)$ contribution. A variety of functional forms have been explored to identify the functions that can provide a

good fit to the data. All the appropriate functions that offer a good fit have been considered in the determination of n_b and the variance of the results arising from the choice of the functional form is adopted as an uncertainty. The procedure is further refined using lattice Quantum Chromodynamics (LQCD) results at low momentum transfers, where neutron data do not exist. In particular, we extracted the ratio G_E^n/G_M^n from numerical simulations within LQCD using the G_E^n and G_M^n data of Ref.³³. The LQCD data provide further guidance on the Q^2 -dependence of the G_E^n/G_M^n ratio based on ab-initio QCD calculations, in a region where neutron form factor data are not available. The LQCD input results to a rather small refinement of ≤ 0.003 in the determination of n_b . The details on the determination of $n_b(Q^2)$ are given in Section 2.1 of the Supplementary Information. The experimentally derived $n_b(Q^2)$ is found in excellent agreement with the theoretical prediction²² as seen in Fig. 1; this in-turn offers further credence to the theoretical effort in Ref.²². Furthermore, the fitted parametrizations allow to constrain the $n_b(Q^2)$ uncertainty by a factor of two compared to the most conservative $n_b = 1.1 \pm 0.1$ (i.e. as indicated by the width of the uncertainty band in Fig. 1), but also to determine these contributions accurately at very low momentum transfers where the analysis of the current TFF data takes place for the G_E^n extraction.

The LQCD results entering our analysis are compared to the experimental world data and they exhibit a very good agreement as shown in Fig. 1a. The parameters of the LQCD calculation are such that they reproduce the physical value of the pion mass. Thus, such a calculation eliminates a major source of systematic uncertainties, that is, the need of a chiral extrapolation. Furthermore, the lattice results include both the connected and disconnected diagrams, and therefore G_E^n and G_M^n include both valence and sea quark contributions.

In our analysis we have extracted the G_E^n under two scenarios; in one case we consider the conservative path where $n_b = 1.1 \pm 0.1$, while in the second we utilize the n_b as we have determined it from the experimental world data. The two sets of results come to an agreement at the $\leq 3\%$ level; this is much smaller than to the overall G_E^n uncertainty. A slightly improved G_E^n uncertainty is obtained in the latter case due to an improved level of the n_b uncertainty, when these contributions are determined from the world data. The G_E^n uncertainty of our results is driven by the following sources: i) Experimental (statistical and systematic) uncertainties in the determination of the $C2/M1$ ratio. ii) Uncertainties in the determination of $C2/M1$ due to the presence of non-resonant pion electro-production amplitudes that interfere with the extraction of the resonant amplitudes. These effects were studied by employing theoretical pion electro-production models in the data analysis; they were further investigated experimentally by measuring $C2/M1$ through an alternative reaction channel, the $p(e, e' p)\gamma$ ²⁸, where one employs a different theoretical framework for the ratio extraction (see Supplementary Information, Section 1). iii) The uncertainty

of the symmetry breaking terms δn_b , as discussed above. iv) The uncertainty introduced by the choice of the G_M^n -parametrization, in order to extract the G_E^n from the G_E^n/G_M^n ratio (as typically done in such cases e.g.^{9,17}). In this work we have used the one from Ref.³⁴ and we have quantified the associated uncertainty by repeating the analysis with alternative parametrizations. We have found a $\sim 0.5\%$ effect, which is rather small compared to the total G_E^n uncertainty. The G_E^n results are displayed in Fig. 3a.

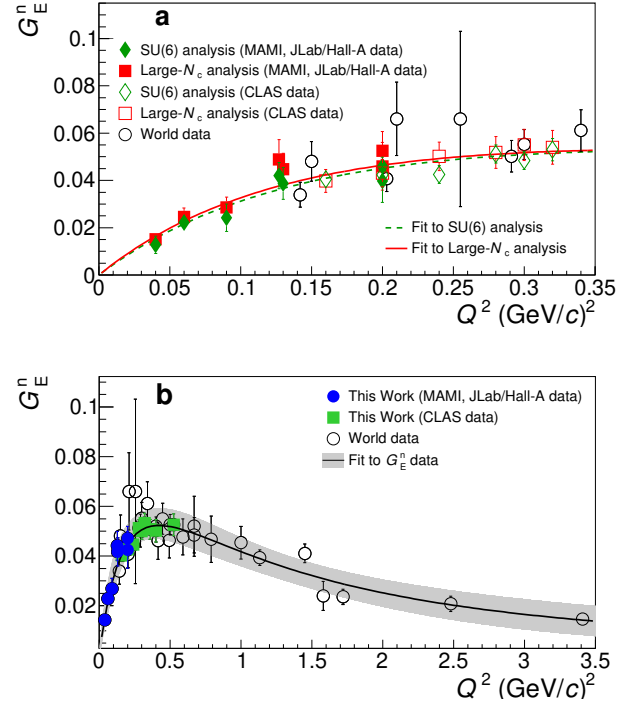


Figure 3. The neutron electric form factor.

a) Green diamonds: the neutron electric form factor, G_E^n , at low momentum transfers from the analysis based on the SU(6)²² and n_b determined from the world data. Red boxes: the G_E^n results from the analysis based on the large- N_c ²³. The fit to the data from the parametrization of Eq. 5 is shown with the dashed and the solid curves, respectively. The filled symbols (diamonds/boxes) correspond to the analysis of the data from Ref.^{24–28} (MAMI, JLab/Hall-A data) and the open ones to that of Ref.³¹ (CLAS data). **b)** Blue circles: The final G_E^n results at low momentum transfers, extracted from the weighted average of the SU(6) and the large- N_c analysis results. The variance of the two data sets is quantified as a theoretical uncertainty. The solid curve shows the fit to the data from the parametrization of Eq. 5, with its uncertainty (shaded band). The G_E^n world data (open-circles)^{7–21} are shown. The extracted G_E^n from the analysis of the CLAS measurements³¹ at intermediate momentum transfers is also shown (green boxes). The error bars correspond to the total uncertainty, at the 1σ or 68% confidence level.

The relation between G_E^n and the quadrupole transition form factors has also been established through large- N_c relations²³. The relations take the form

$$\frac{E2}{M1}(Q^2) = \left(\frac{M_N}{M_\Delta}\right)^{3/2} \frac{M_\Delta^2 - M_N^2}{2Q^2} \frac{G_E^n(Q^2)}{F_2^p(Q^2) - F_2^n(Q^2)} \quad (2)$$

$$\frac{C2}{M1}(Q^2) = \left(\frac{M_N}{M_\Delta}\right)^{3/2} \frac{Q_+ Q_-}{2Q^2} \frac{G_E^n(Q^2)}{F_2^p(Q^2) - F_2^n(Q^2)} \quad (3)$$

where $F_2^{p(n)}$ are the nucleon Pauli form factors, M_Δ is the mass of the Δ , and $Q_\pm = ((M_\Delta \pm M_N)^2 + Q^2)^{1/2}$. Here one is free from any additional correction terms, such as the symmetry breaking contributions of Eq. 1. Another advantage is that the experimental database is extended to include the Electric quadrupole (E2) transition, which in turn allows for an improved extraction of G_E^n . Being able to extract G_E^n independently through the Coulomb and the Electric quadrupole transitions offers a strong experimental test to the validity of the large- N_c relations and allows to quantify their level of theoretical uncertainty. The above relations come with a 15% theoretical uncertainty²³ that is treated accordingly in the G_E^n analysis. The G_E^n extraction from the Coulomb and from the Electric quadrupole transitions agree nicely within that level, as can be seen in Fig. 1b, and validate this level of uncertainty. For the well-known G_E^p , G_M^p and G_M^n that enter in the expressions through the Pauli form factors we have used recent parametrizations. For the G_M^p and G_M^n we used Ref.³⁴. For G_E^p we performed an updated parametrization so that we may include recent measurements from Ref.³⁵ that were not yet available in Ref.³⁴ (see Supplementary Information, Section 4). For the large- N_c analysis the final results integrate both of the quadrupole transition form factors from each experiment, when both of them were simultaneously measured, into one G_E^n measurement (see Supplementary Information, Section 2.2). The extracted G_E^n results from the large- N_c analysis are displayed in Fig. 3a and are compared to the results from the SU(6) analysis in the same figure. The SU(6) analysis is in agreement with the large- N_c analysis G_E^n results. For our final G_E^n result we consider the weighted average of the two values, as shown in Fig. 3b. The variance of the two values is treated as an additional G_E^n theoretical uncertainty, and is accounted for accordingly in the $\langle r_n^2 \rangle$ extraction.

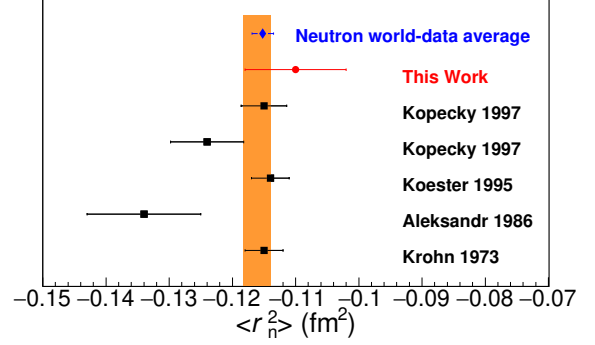


Figure 4. The neutron mean square charge radius.

The $\langle r_n^2 \rangle$ measurement from this work (red circle), with the error bar corresponding to the total uncertainty at the 1σ or 68% confidence level, and from references³⁻⁶ (black box) included in the PDG analysis for $\langle r_n^2 \rangle$. The orange-band indicates the PDG averaged $\langle r_n^2 \rangle$ value. The new weighted average of the world data is also shown (blue diamond) when the new $\langle r_n^2 \rangle$ measurement reported in this work is included in the calculation.

The neutron mean square charge radius is related to the slope of the neutron electric form factor as $Q^2 \rightarrow 0$ through

$$\langle r_n^2 \rangle = -6 \frac{dG_E^n(Q^2)}{dQ^2} \Big|_{Q^2 \rightarrow 0}. \quad (4)$$

In order to determine the charge radius the data have to be fitted to a functional form, and the slope has to be determined at $Q^2 = 0$. It is important that a proper functional form is identified so that model dependent biases to the fit are avoided. In the past, the experimental data would allow to explore functional forms for $G_E^n(Q^2)$ with only two free parameters, that were lacking the ability to determine the neutron charge radius. The updated data allow to introduce an additional free parameter and to extract the $\langle r_n^2 \rangle$ from measurements of the G_E^n that was not possible previously. Our studies have shown that

$$G_E^n(Q^2) = (1 + Q^2/A)^{-2} \frac{B\tau}{1 + C\tau}, \quad (5)$$

is the most robust function for the radius extraction, where $\tau = Q^2/4M_N^2$, and A, B, C are free parameters (see Supplementary Information, Section 3). Our fits employ the G_E^n data discussed in this work as well as the G_E^n world data from⁷⁻²¹. The function describes the data very well, with a reduced χ^2 of 0.74. The parameters obtained are $A = 0.505 \pm 0.079$ (GeV/c)², $B = 1.655 \pm 0.126$, $C = 0.909 \pm 0.583$, and Q^2 in units of (GeV/c)², leading to a value of $\langle r_n^2 \rangle = -0.110 \pm 0.008$ (fm²), as shown in Fig. 4. When the uncertainty of the symmetry breaking contributions in the SU(6) analysis is treated conservatively (i.e. $n_b = 1.1 \pm 0.1$) the final result becomes $\langle r_n^2 \rangle = -0.109 \pm 0.009$ (fm²) with a reduced χ^2 of 0.74. Here we observe that the $\langle r_n^2 \rangle$ -uncertainty

is not affected significantly by the different treatment of the symmetry breaking contributions in the two cases.

The charge radius extraction is further explored through fits that are constrained within a limited range at low Q^2 where G_E^n remains monotonic, namely from $Q^2 = 0$ to $0.4 \text{ (GeV}/c)^2$. In the fits to the data, the functional forms can be divided into two groups, those based on polynomials with varying orders and those that are based on rational forms (see Supplementary Information, Section 3.1). For the charge radius, the weighted average is extracted separately for each one of the two groups. A systematic uncertainty is also quantified within each group (i.e. a model uncertainty of the group) from the weighted variance of the results from all the fits within the group. The results from the two groups tend to have a similar overall uncertainty. A small systematic difference of the two group's central $\langle r_n^2 \rangle$ values is observed, as studies over a varying fitting range have shown. For that reason a third uncertainty is determined: here we consider the spread of the two central values as indicative of the uncertainty that is associated with the choice of the group. Therefore, the final result is given by the average of the two group values for $\langle r_n^2 \rangle$, while the half of the difference of the two values is assigned as an additional uncertainty. The details of the studies are presented in the Supplementary Information, Sections 3.1 and 3.2. The results from the low- Q^2 fits for all groups of functions and for variations to the fitting range are shown in the Supplementary Information, Tab.7 and Tab.8. The low- Q^2 fits confirm the $\langle r_n^2 \rangle$ extraction from the fits over the complete G_E^n database, but they are vulnerable to model uncertainties that are associated with the choice of the fitted parametrization and they are not able to improve the $\langle r_n^2 \rangle$ extraction. The studies indicate that more G_E^n measurements are needed at lower momentum transfers so that a more competitive extraction can become possible from the low- Q^2 fits. This comes as no surprise when one considers the corresponding case for the proton, in which case the charge radius extraction from fits within a limited Q^2 -range required measurements at significantly smaller momentum transfers, namely at $Q^2 = 0.0002 \text{ (GeV}/c)^2 - 0.06 \text{ (GeV}/c)^2$ ³⁵.

The quadrupole TFF data at low momentum transfers ^{24–28}, acquired at MAMI and at JLab/Hall-A, provide the critical G_E^n data that were missing lower than $Q^2 = 0.20 \text{ (GeV}/c)^2$ and make the $\langle r_n^2 \rangle$ extraction possible. We now explore the potential of extending the current analysis to higher momentum transfers. This study aims to observe the effect of the $\langle r_n^2 \rangle$ extraction if we enrich the G_E^n database with measurements in the region where G_E^n data already exist, higher than $Q^2 = 0.20 \text{ (GeV}/c)^2$. The relations between the G_E^n and the quadrupole transition form factors hold on very solid ground in the low Q^2 region, i.e., lower than $Q^2 = 0.20 \text{ (GeV}/c)^2$. On the other hand, they tend to hold less well at high momentum transfers. The relations do not come with a sharp Q^2 cut-off-value after which they do not hold, but one should avoid the $Q^2 = 1 \text{ (GeV}/c)^2$ region

where larger theoretical uncertainties could bias the charge radius extraction. In extending the database higher in Q^2 , care has to be given so that any additional data at intermediate momentum transfers will benefit the fits without compromising the $\langle r_n^2 \rangle$ extraction by the gradually increasing theoretical uncertainties. Our studies showed that when we integrate in the analysis the G_E^n data that we extract from the CLAS measurements up to $Q^2 = 0.52 \text{ (GeV}/c)^2$ ³¹ (see Fig. 3b, green boxes) we find that $\langle r_n^2 \rangle = -0.107 \pm 0.007 \text{ (fm}^2\text{)}$, compared to $\langle r_n^2 \rangle = -0.110 \pm 0.008 \text{ (fm}^2\text{)}$ when these additional data are not included (see the Supplementary Information, Section 3.2 for details). Lastly, when the same data-set is included in the fits within the limited low- Q^2 range, as discussed in the previous paragraph, we find that $\langle r_n^2 \rangle = -0.111 \pm 0.006 \pm 0.002_{\text{mod}} \pm 0.004_{\text{group}} \text{ (fm}^2\text{)}$. Here the last two uncertainties (mod and group) are model-related uncertainties associated with the choice of the fitted parametrization (see Supplementary Information, Section 3.2 for details). We do not observe any additional benefit by extending the measurements higher in Q^2 since the fits' uncertainties do not improve when more data are included up to $Q^2 = 1 \text{ (GeV}/c)^2$. In conclusion, a small benefit to the charge radius uncertainty can be observed when additional data up to $Q^2 = 0.5 \text{ (GeV}/c)^2$ are utilized for the charge radius extraction. If one decides to eliminate any risk of introducing theoretical bias from the inclusion of the intermediate momentum transfer measurements for the final result, one can conservatively adopt the analysis that does not include these additional data, namely $\langle r_n^2 \rangle = -0.110 \pm 0.008 \text{ (fm}^2\text{)}$.

Discussion

Our analysis and results offers valuable input towards addressing long standing unresolved $\langle r_n^2 \rangle$ discrepancies of the b_{ne} -measurements, which display a $\approx 10\%$ tension between the results, suggesting that there are still unidentified systematic uncertainties associated with this method of extraction. Our measurement is in disagreement with Ref. ⁵ and supports the results of Ref. ^{3,4}. Considering that here we cross check $\langle r_n^2 \rangle$ using a different extraction method, there is a strong argument so as to exclude the value of Ref. ⁵ from the world data average. In such a case, the new weighted average value of the world data when we include our measurement and we exclude the one of Ref. ⁵, becomes $\langle r_n^2 \rangle = -0.1152 \pm 0.0017 \text{ (fm}^2\text{)}$. Based on the current work, the particle data book value of $\langle r_n^2 \rangle = -0.1161 \pm 0.0022 \text{ (fm}^2\text{)}$ is adjusted by $\sim 1\%$ and improves its uncertainty by $\sim 23\%$. We also note that our result agrees very well with a recent $\langle r_n^2 \rangle$ calculation that is based on the determination of the deuteron structure radius in chiral effective field theory and utilizes atomic data for the difference of the deuteron and proton charge radii ³⁶.

The neutron's non-zero mean charge radius is a direct consequence of the asymmetric distribution of the positively-charged (up) and of the negatively-charged (down) quarks in the system, a consequence of the non-trivial quark gluon

dynamics of the strong force. The quark distributions offer a detailed view as to how the non-zero $\langle r_n^2 \rangle$ value arises. Here, one has to work on the infinite-momentum frame³⁷ since it offers the inherent advantage that a true transverse charge density can be properly defined as the matrix element of a density operator between identical initial and final states. We find that the results of our analysis on $\langle r_n^2 \rangle$ are particularly sensitive to the neutron's long-distance structure, and offer a significant improvement (factor of 2) in the precision of the neutron charge density at its surface (see Supplementary Information Fig. 9). We extract the neutron and the proton charge densities at the infinite-momentum-frame from the most recent nucleon form factor parametrizations, where for G_E^n we use the one determined in this work. The details are presented in the Supplementary Information, Section 4. The extracted neutron and proton charge densities are shown in Fig. 5. From the two nucleon densities, invoking charge symmetry, and neglecting the $s\bar{s}$ contribution, we derive the u - and d -quark densities with an improved precision as shown in Fig. 5 (see Supplementary Information, Section 4 for details). The flavor dependent densities show that the singly-represented quark in the nucleon has a wider distribution compared to the doubly-represented quarks, which in turn exhibit a larger central quark density. Although the concentration of the two negatively charged quarks at the center of the neutron may appear to contradict the negative sign of the neutron's mean square charge radius, this is not truly the case. The 3D Breit frame and 2D infinite-momentum distributions are directly related to each other and the apparent discrepancies between the distributions in the two frames simply result from kinematical artifacts associated with spin³⁸. The effect is rather dramatic in the neutron, where the rest-frame magnetization is large and negative. The contribution it induces competes with the convection contribution and gradually changes the sign at the center of the charge distribution as one increases the momentum of the neutron. Thus, the appearance of a negative region around the center of the neutron charge distribution in the infinite-momentum frame is just a manifestation of the contribution induced by the rest-frame magnetization.

In conclusion, we report on an alternative measurement of the neutron charge radius, based on the measurement of the neutron electric form factor G_E^n . An alternative path to the measurements based on the scattering of neutrons by electrons bound in diamagnetic atoms is presented. Our value of $\langle r_n^2 \rangle = -0.110 \pm 0.008 \text{ (fm}^2\text{)}$ offers valuable input towards addressing long standing unresolved discrepancies in the $\langle r_n^2 \rangle$ measurements, rejects earlier measurements, and improves the precision of the $\langle r_n^2 \rangle$ world data average value. Furthermore, our data offer access to the associated dynamics of the strong nuclear force through the precise mapping of the quark distributions in the neutron that contribute to its non-zero charge radius. The current work lays the path for $\langle r_n^2 \rangle$ measurements of higher precision. New experimental proposals based on this method, e.g. Jefferson Lab LOI 12-20-002,

offer to improve the precision of the $\langle r_n^2 \rangle$ measurement by nearly a factor of 2. Future experimental efforts will be able to utilize upgraded experimental setups that will fully exploit the advantages of this method. In particular, pushing the low momentum transfer limits of high precision measurements can lead to a further improvement in the precision of the $\langle r_n^2 \rangle$ extraction.

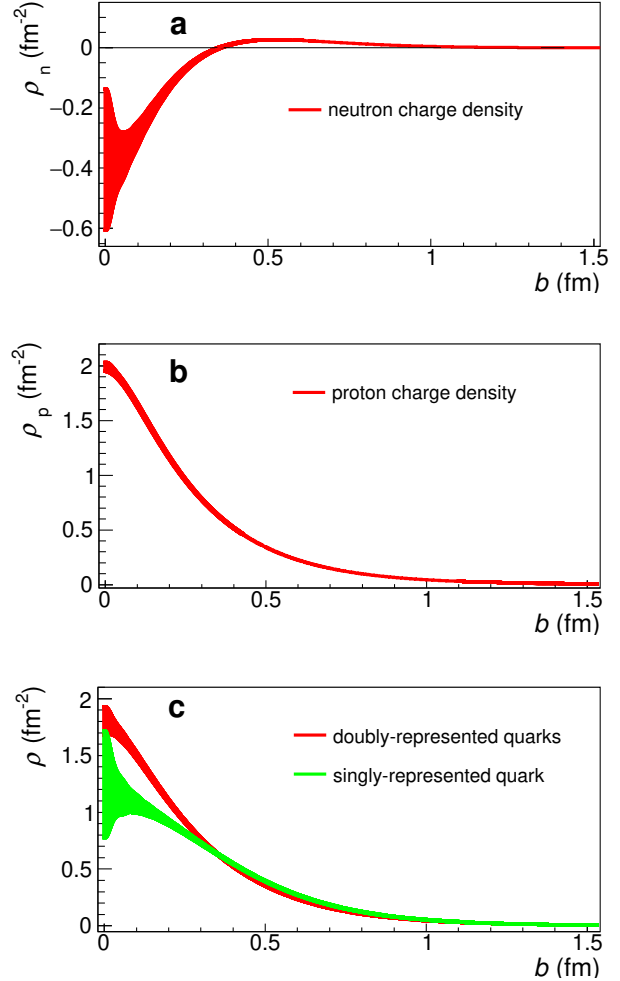


Figure 5. The nucleon charge densities.

a) The neutron charge density ρ_n . **b)** The proton charge density ρ_p . **c)** Flavor decomposition of the nucleon charge densities: the doubly-represented (red) and singly-represented (green) charge densities in the nucleon. Each is normalized to unity.

Methods

Here we extract G_E^n , at low momentum transfers, from measurements of the quadrupole transition form factors. The neutron charge radius is then extracted from the slope of G_E^n at $Q^2 = 0$. Utilizing the G_E^n data and the world data for the nucleon elastic form factors the flavor decomposition of the

nucleon electromagnetic form factors is performed, and the u - and d -quark distributions in the nucleon are extracted. The main steps of this work are as follows:

1. We extract G_E^n from the Coulomb quadrupole and the Electric quadrupole transition form factor data at low momentum transfers^{24–27} utilizing the form factor relations (Eqs. 1, 2, and 3) that have been determined within the SU(6)²² and the large- N_c ²³ frameworks. The symmetry breaking corrections, $n_b(Q^2)$, in Eq. 1 are determined experimentally from the world data (elastic neutron form factors and $N \rightarrow \Delta$ transition form factors) and are further refined using state of the art Lattice QCD calculations. Parametrizations are used for the well known G_E^p , G_M^p and G_M^n form factors. Multiple parametrizations are employed so as to quantify the corresponding uncertainty introduced into the G_E^n extraction.
2. The final G_E^n values are extracted by the weighted average of the SU(6)²² and the large- N_c ²³ analysis results. The variance between the results of the two methods is treated as a theoretical uncertainty.
3. The neutron mean square charge radius $\langle r_n^2 \rangle$ is obtained from Eq. 4 by fitting the G_E^n data to the functional form in Eq. 5 and determining the slope at $Q^2 = 0$. This functional form was shown to be the most robust function for the radius extraction from the neutron data. The fit employs additional G_E^n data reported here and the G_E^n world data extending to higher momentum transfers.
4. The neutron and proton densities are derived at the infinite momentum frame through

$$\rho(b) = \int_0^\infty \frac{dQ}{2\pi} Q J_0(Qb) \frac{G_E(Q^2) + \tau G_M(Q^2)}{1 + \tau} \quad (6)$$

where b is the transverse distance, $\tau = Q^2/4m^2$ and J_0 the 0th order cylindrical Bessel function. Here we utilize the most recent parametrizations for the nucleon form factors, where for G_E^n we use the one derived in this work. From the neutron and proton densities, invoking charge symmetry, and neglecting the $s\bar{s}$ contribution, we then extract the u - and d -quark densities in the proton (or doubly-represented and singly-represented quarks in the nucleon, respectively), where

$$\rho_u(b) = \rho_p(b) + \rho_n(b)/2 \quad (7)$$

and

$$\rho_d(b) = \rho_p(b) + 2\rho_n(b). \quad (8)$$

Data availability

All the relevant data in this work are available from the authors upon request. The data for the quadrupole TFFs

used in this work are publicly available in their original publications^{24–28,31} where they are described in detail. The raw data from these experiments are archived in Jefferson Laboratory’s mass storage silo and at Temple University, Department of Physics. The G_E^n data that we have used for the $\langle r_n^2 \rangle$ extraction are available in the following sources: i) The new G_E^n data that we have derived in this work, from the analysis of the quadrupole TFFs, are available in the Supplementary Information document. ii) The previously published G_E^n world-data are available in their original publications^{7–21}.

Code availability

The data analysis uses the standard C++ ROOT framework, which was developed at CERN and is freely available at <https://root.cern.ch>. The computer codes used for the data analysis and for the generation of plots are available upon request.

References

1. Pohl, R. *et al.* The size of the proton. *Nature* **466**, 213–216 (2010).
2. R. Pohl, G. A. M., R. Gilman & Pachucki, K. Muonic hydrogen and the proton radius puzzle. *Ann. Rev. Nucl. Part. Sci.* **63**, 175–204 (2013).
3. Kopecky, S. *et al.* Neutron charge radius determined from the energy dependence of the neutron transmission of liquid Pb-208 and Bi-209. *Phys. Rev.* **C56**, 2229–2237 (1997).
4. Koester, L. *et al.* Neutron electron scattering length and electric polarizability of the neutron derived from cross-sections of bismuth and of lead and its isotopes. *Phys. Rev.* **C51**, 3363–3371 (1995).
5. Aleksandrov, Yu. A., Vrana, M., Manrique, G. J., Machekhina, T. A. & Sedlakova, L. N. Neutron rms radius and electric polarizability from data on the interaction of slow neutrons with bismuth. *Sov. J. Nucl. Phys.* **44**, 900–902 (1986).
6. Krohn, V. E. & Ringo, G. R. Reconsiderations of the electron - neutron scattering length as measured by the scattering of thermal neutrons by noble gases. *Phys. Rev.* **D8**, 1305–1307 (1973).
7. Madey, R. *et al.* Measurements of G_E^n/G_M^n from the $^2H(\vec{e}, e'\vec{n})^1H$ reaction to $Q^2 = 1.45$ (GeV/c)². *Phys. Rev. Lett.* **91**, 122002 (2003).
8. Schlimme, B. S. *et al.* Measurement of the neutron electric to magnetic form factor ratio at $Q^2 = 1.58$ GeV² using the reaction $^3He(\vec{e}, e'n)pp$. *Phys. Rev. Lett.* **111**, 132504 (2013).
9. Riordan, S. *et al.* Measurements of the Electric Form Factor of the Neutron up to $Q^2=3.4$ GeV² using the Reaction $^3He(\vec{e}, e'n)pp$. *Phys. Rev. Lett.* **105**, 262302 (2010).

10. Glazier, D. I. *et al.* Measurement of the electric form-factor of the neutron at $Q^2 = 0.3$ (GeV/c)² to 0.8 (GeV/c)². *Eur. Phys. J.* **A24**, 101–109 (2005).
11. Plaster, B. *et al.* Measurements of the neutron electric to magnetic form-factor ratio G_{En}/G_{Mn} via the ${}^2H(\vec{e}, e', \vec{n})^1H$ reaction to $Q^2 = 1.45$ (GeV/c)². *Phys. Rev.* **C73**, 025205 (2006).
12. Zhu, H. *et al.* A Measurement of the electric form-factor of the neutron through $\vec{d}(\vec{e}, e'n)p$ at $Q^2 = 0.5$ (GeV/c)². *Phys. Rev. Lett.* **87**, 081801 (2001).
13. Warren, G. *et al.* Measurement of the electric form-factor of the neutron at $Q^2 = 0.5$ and 1.0 GeV²/c². *Phys. Rev. Lett.* **92**, 042301 (2004).
14. Rohe, D. *et al.* Measurement of the neutron electric form-factor $G_{(en)}$ at 0.67(GeV/c)² via ${}^3He(\vec{e}, e'n)$. *Phys. Rev. Lett.* **83**, 4257–4260 (1999).
15. Passchier, I. *et al.* The Charge form-factor of the neutron from the reaction polarized ${}^2H(\vec{e}, e, e'n)p$. *Nucl. Phys. A* **663**, 421–424 (2000).
16. Bermuth, J. *et al.* The Neutron charge form-factor and target analyzing powers from ${}^3He(\vec{e}, e'n)$ scattering. *Phys. Lett.* **B564**, 199–204 (2003).
17. Geis, E. *et al.* The Charge Form Factor of the Neutron at Low Momentum Transfer from the ${}^2H(\vec{e}, e'n)p$ Reaction. *Phys. Rev. Lett.* **101**, 042501 (2008).
18. Eden, T. *et al.* Electric form factor of the neutron from the ${}^2H(\vec{e}, e'n)^1H$ reaction at $Q^2=0.255$ (GeV/c)². *Phys. Rev. C* **50**, R1749–R1753 (1994).
19. Ostrick, M. *et al.* Measurement of the Neutron Electric Form Factor $G_{E,n}$ in the Quasifree ${}^2H(\vec{e}, e' \vec{n})p$ Reaction. *Phys. Rev. Lett.* **83**, 276–279 (1999).
20. Golak, J., Ziemer, G., Kamada, H., Witała, H. & Glöckle, W. Extraction of electromagnetic neutron form factors through inclusive and exclusive polarized electron scattering on a polarized 3He target. *Phys. Rev. C* **63**, 034006 (2001).
21. Herberg, C. *et al.* Determination of the neutron electric form-factor in the D(e,e' n)p reaction and the influence of nuclear binding. *Eur. Phys. J.* **A5**, 131–135 (1999).
22. Buchmann, A. J. Electromagnetic N \rightarrow Δ transition and neutron form-factors. *Phys. Rev. Lett.* **93**, 212301 (2004).
23. Pascalutsa, V. & Vanderhaeghen, M. Large- N_c relations for the electromagnetic nucleon-to- Δ form factors. *Phys. Rev.* **D76**, 111501(R) (2007).
24. Blomberg, A. *et al.* Electroexcitation of the $\Delta^+(1232)$ at low momentum transfer. *Phys. Lett.* **B760**, 267–272 (2016).
25. Stave, S. *et al.* Lowest Q^2 Measurement of the $\gamma^* p \rightarrow \Delta$ Reaction: Probing the Pionic Contribution. *Eur. Phys. J.* **A30**, 471–476 (2006).
26. Sparveris, N. *et al.* Measurements of the $\gamma^* p \rightarrow \Delta$ reaction at low Q^2 . *Eur. Phys. J.* **A49**, 136 (2013).
27. Sparveris, N. F. *et al.* Determination of quadrupole strengths in the $\gamma^* p \rightarrow \Delta(1232)$ transition at $Q^2 = 0.20$ (GeV/c)². *Phys. Lett.* **B651**, 102–107 (2007).
28. Blomberg, A. *et al.* Virtual Compton Scattering measurements in the nucleon resonance region. *Eur. Phys. J. A* **55**, 182 (2019). [1901.08951](https://doi.org/10.1007/s00034-019-08951-1).
29. Sparveris, N. F. *et al.* Investigation of the conjectured nucleon deformation at low momentum transfer. *Phys. Rev. Lett.* **94**, 022003 (2005).
30. Elsner, D. *et al.* Measurement of the LT-asymmetry in π^0 electroproduction at the energy of the $\Delta(1232)$ resonance. *Eur. Phys. J.* **A27**, 91–97 (2006).
31. Aznauryan, I. G. *et al.* Electroexcitation of nucleon resonances from CLAS data on single pion electroproduction. *Phys. Rev.* **C80**, 055203 (2009).
32. Kelly, J. J. *et al.* Recoil polarization measurements for neutral pion electroproduction at $Q^2 = 1$ (GeV/c)² near the Delta resonance. *Phys. Rev.* **C75**, 025201 (2007).
33. Alexandrou, C. *et al.* Proton and neutron electromagnetic form factors from lattice QCD. *Phys. Rev.* **D100**, 014509 (2019).
34. Ye, Z., Arrington, J., Hill, R. J. & Lee, G. Proton and Neutron Electromagnetic Form Factors and Uncertainties. *Phys. Lett.* **B777**, 8–15 (2018).
35. Xiong, W. *et al.* A small proton charge radius from an electron–proton scattering experiment. *Nature* **575**, 147–150 (2019).
36. Filin, A. A. *et al.* Extraction of the Neutron Charge Radius from a Precision Calculation of the Deuteron Structure Radius. *Phys. Rev. Lett.* **124**, 082501 (2020).
37. Miller, G. A. Charge Density of the Neutron and Proton. *Phys. Rev. Lett.* **99**, 112001 (2007).
38. Lorce, C. Charge Distributions of Moving Nucleons. *Phys. Rev. Lett.* in press, [arXiv:2007.05318](https://arxiv.org/abs/2007.05318) (2020).

Acknowledgements

We would like to thank M. Vanderhaeghen as this work received great benefit from his input and suggestions. This work has been supported by the US Department of Energy Office of Science, office of Nuclear Physics under contract no. DE-SC0016577, DE-FG02-94ER40844 and DEAC02-06CH11357. M.C. acknowledges financial support by the U.S. Department of Energy, Office of Nuclear Physics, Early Career Award under Grant No. DE-SC0020405.

Author contributions

N.S. and Z.-E.M. guided and supervised this effort. N.S. lead the experimental program at JLab (Hall A) and at MAMI (A1) that resulted to the new G_E^n measurements (experiment spokesperson and analysis coordinator). H.A. and M.P. performed the fits, and the extraction of the charge densities and radii. M.C. was in charge of the LQCD results and supervised theoretical aspects of this work.

Competing interests

The authors declare no competing interests.

Supplementary information

Supplementary information is available for this paper.

Correspondence and request of materials

Correspondence and request of materials should be addressed to N.S.

Supplementary Information

Measurement of the neutron charge radius and the role of its constituents

H. Atac¹, M. Constantinou¹, Z.-E. Meziani^{2,1}, M. Paolone³, and N. Sparveris^{1,*}

¹Temple University, Philadelphia, PA 19122, USA

²Argonne National Laboratory, Lemont, IL 60439, USA

³New Mexico State University, Las Cruces, NM 88003, USA

*e-mail: sparveri@temple.edu

Table of Contents

Section		Page
1	Description of the quadrupole transition form factor measurements	3
2	Extraction of G_E^n	3
2.1	Analysis within SU(6)	4
2.2	Analysis within large- N_c	7
3	Neutron charge radius extraction	9
3.1	Extraction from fits within a limited low- Q^2 range	10
3.2	Extraction including additional data at higher Q^2	12
3.2.1	Considerations on the CLAS data uncertainties	14
4	Flavor dependent charge densities	15
5	Lattice QCD results	15

In this document, we present details regarding to the analysis steps and the results reported in this work. More specifically we discuss: the experimental data of the quadrupole transition form factors and the nature of their uncertainties that enter into the G_E^n extraction; the steps for the G_E^n extraction from the transition form factors; the extraction procedure for $\langle r_n^2 \rangle$; the extraction of the flavor dependent form factors, densities, and mean square radii; the Lattice QCD results. Detailed tables with all the parametrizations and the final results are given, as well as additional figures that are constructive towards the discussion of this work.

1 Description of the quadrupole transition form factor measurements

The neutron electric form factor G_E^n has been extracted from measurements of the $N \rightarrow \Delta$ quadrupole transition form factors in the four-momentum transfer squared range $Q^2 = 0.04 \text{ (GeV}/c)^2$ to $Q^2 = 0.20 \text{ (GeV}/c)^2$. The main aspects of these measurements that are relevant within the context of the current work are briefly described in this section, and for an extensive description of the experimental details we refer to¹⁻⁵. The measurements involve a coordinated experimental program, at JLab (Hall A) and at MAMI (A1), where:

- The experiments shared the same methodology, experimental setup specifications, and analysis tools and procedures.
- The two experimental setups offer complementarity in their kinematical coverage of momentum transfer, and the measurements were coordinated accordingly so that the low- Q^2 region is optimally measured.
- Measurements at common kinematics have been performed (i.e. at $Q^2 = 0.13 \text{ (GeV}/c)^2$ see Refs.^{1,3}) so that a cross check between the results from the two experimental setups is made, and consistency is ensured.
- A first measurement through the $p(e, e' p)\gamma$ channel⁵ has been performed so that a comparison to the pion-electroproduction results¹⁻⁴ can be made. Such a comparison offers critical input towards the model uncertainty of the world data. For optimal comparison, the measurements were performed at the same Q^2 and with the same experimental setup for both channels.

More specifically, in both experiments an electron beam with energy $E \approx 1 \text{ GeV}$ has been employed on a liquid hydrogen target, and two high resolution spectrometers are used to detect protons and electrons in coincidence for the measurement of the pion electro-production excitation channel. Both setups offer a spectrometer momentum resolution of 10^{-4} , and a coincidence-time resolution between the proton and the electron spectrometers of $\approx 1 \text{ ns}$. The experimental setup offers high resolution i.e. the spectrometers focus within a very well defined bin of the kinematical phase space, and high precision cross section measurements are performed sequentially until the extended phase space has been covered (as opposed to different techniques where e.g. detectors with larger (4π) acceptance coverage but of reduced resolution are employed⁶).

An important aspect of this experimental program is the consistent, and extensive, treatment of the non-resonant pion electro-production amplitudes that interfere with the extraction of the resonant amplitudes in the $N \rightarrow \Delta$ transition. These interfering contributions, small in magnitude but large in number, can not be sufficiently constrained by the experimental measurements, and they thus result into a model uncertainty for the quadrupole transition form factors. In the past these contributions have been frequently poorly studied and rarely quoted as an uncertainty. Here, the effect of these amplitudes has been studied in the following manner:

- (a) State of the art theoretical pion electroproduction models⁷⁻¹¹ have been employed in the data analysis. The models offer different descriptions for the background amplitudes, leading to deviations in the extracted values of the transition form factors that are quantified as a model uncertainty. This uncertainty is in turn appropriately treated in the extraction of the G_E^n .
- (b) The above model uncertainties are determined within the pion electroproduction framework. However, the excitation can also be studied through the weak $p(e, e' p)\gamma$ channel. In this case the same physics signal can be extracted within a different theoretical framework, thus offering an ideal cross-check to the model uncertainties associated with the pion electroproduction channel. The branching ratio of the photon channel is very small (0.6%), two orders of magnitude smaller compared to the pion-electroproduction, and as such it was not studied until recently. To that end, the first such measurement was conducted at MAMI (A1)⁵. Measurements at the same Q^2 , utilizing the same experimental setup, were performed. The results were found in agreement between the two channels^{4,5}, thus giving credence to the quantification of the model uncertainties.

2 Extraction of G_E^n

The G_E^n is extracted from the quadrupole transition form factor measurements¹⁻⁵ utilizing the form factor relations^{12,13} determined within the SU(6) and the large- N_c frameworks. The data are analyzed independently within the two frameworks. The weighted average of the two values leads to the final G_E^n and the variance of the two values is assigned as a G_E^n theoretical

uncertainty, that is accounted for accordingly in the r_n extraction. In order to extract G_E^n from the G_E^n/G_M^n we utilize a parametrization of the well known G_M^n (as typically done in such cases, e.g.^{14,15} etc). In this work we have used the recent parametrization¹⁶. The uncertainties associated with the G_E^n extraction are the following:

- Experimental (statistical and systematic) uncertainties of the quadrupole amplitudes.
- Model uncertainties of the quadrupole amplitudes (not applicable to measurement⁵).
- The theoretical uncertainty associated with the relations in^{12,13}.
- The uncertainty due to the G_M^n parametrization.

The uncertainty introduced by G_M^n has been studied by employing different G_M^n -parametrizations to the G_E^n extraction. For that we have used the most recent¹⁶, the widely adopted in the past¹⁷, as well as a parametrization that we worked out towards that end. The overall effect to G_E^n has been quantified $\approx 0.5\%$, and is rather small compared to the total uncertainty.

2.1 Analysis within SU(6)

A consequence of the SU(6) spin and flavor symmetry group in which the nucleon and the Δ resonance belong leads to the following expression¹²

$$\frac{G_E^n(Q^2)}{G_M^n(Q^2)} = \frac{Q}{|\mathbf{q}|} \frac{2Q}{M_N} \frac{1}{n_b(Q^2)} \frac{C2}{M1}(Q^2) \quad (1)$$

where $|\mathbf{q}|$ is the virtual photon three-momentum transfer magnitude in the γN center of mass frame, M_N is the nucleon mass, and n_b describes three-quark current terms that slightly increase the C2/M1 ratio (or correspondingly decrease the G_E^n/G_M^n), an SU(6) symmetry breaking correction that has been theoretically quantified to $\approx 10\%$ ¹² (i.e. $n_b \approx 1.1$).

The data have been analyzed in two ways:

i) Following the most conservative path, a theoretical uncertainty can be assigned that is equal to the full magnitude of the symmetry breaking contributions i.e. $n_b = 1.1 \pm 0.1$. Considering the confidence with which the underlying theory is able to determine the level of the symmetry breaking contributions, the above assumption leads to a safe estimation, and most likely to an overestimation, of the theoretical uncertainty.

ii) The wealth of the experimental world data for $C2/M1$ ^{1-6,18-20} and for G_E^n/G_M^n ^{14,15,21-32} allow to determine the magnitude of the symmetry breaking corrections¹. Refinements to the corrections are implemented utilizing the LQCD data for G_E^n/G_M^n reported in this work (see later in the LQCD section).

The results from (i) and (ii) are in excellent agreement; the difference between the analysis (i) and (ii) results to a very small effect in the r_n extraction (see the radius extraction section). This comes as a consequence of the confirmation of the n_b theoretical prediction¹² by the experimental data (see Fig. 1). The experimental determination of the breaking corrections n_b takes place as follows:

First, we determine the set of appropriate functions $F_R(Q^2)$ that can successfully parametrize the G_E^n/G_M^n ratio. To that end we have identified the following forms that are able to provide a good fit to the data:

$$F_R(x) = \sum_{i=1}^j a_i x_i^i, \quad F_R(x) = \frac{\sum_{i=1}^j b_i x_i^i}{(1 + \sum_{j=1}^j c_j x_j^j)}, \quad F_R(x) = (1 - \exp(-d_1 x)).$$

For each one of these functions:

- The $F_R(Q^2)$ parametrization is determined by fitting to the G_E^n/G_M^n world data^{14,15,21-32}.
- The $F_R^*(Q^2)$ is determined by fitting to the G_E^n/G_M^n ratios as derived from the $N \rightarrow \Delta$ measurements^{1-6,18-20} through Eq. 1 for $n_b=1$.
- The breaking corrections are then determined, for each functional form, through: $n_b(Q^2) = F_R^*(Q^2)/F_R(Q^2)$.

¹A revised analysis of the² has updated the C2/M1 result to $(-4.10 \pm 0.27_{\text{stat+sys}} \pm 0.26_{\text{mod}})\%$

	$\sum_{i=1}^i a_i x_i^i$		$\frac{\sum_{i=1}^i b_i x_i^i}{(1 + \sum_{j=1}^j c_j x_j^j)}$				$(1 - \exp^{(d_1 x)})$
$F_R(x)$							
a_1	1.420	1.670	-	-	-	-	-
a_2	-2.351	-5.962	-	-	-	-	-
a_3	-	10.968	-	-	-	-	-
b_1	-	-	1.679	16.050	1.790	11.236	-
b_2	-	-	14.840	11.590	20.340	0.802	-
b_3	-	-	-	15.168	0.801	15.168	-
b_4	-	-	-	-	-	43.971	-
c_1	-	-	13.602	43.980	18.111	1.756	-
c_2	-	-	31.396	1.757	49.377	16.089	-
c_3	-	-	-	-	-40.446	-	-
d_1	-	-	-	-	-	-	-0.336
$F_R^*(x)$							
a_1	1.587	1.707	-	-	-	-	-
a_2	-2.243	-4.349	-	-	-	-	-
a_3	-	6.078	-	-	-	-	-
b_1	-	-	1.851	0.170	1.919	12.346	-
b_2	-	-	2.495	15.730	23.081	0.800	-
b_3	-	-	-	3.455	0.801	15.369	-
b_4	-	-	-	-	-	35.134	-
c_1	-	-	6.090	15.298	18.943	1.904	-
c_2	-	-	-0.955	1.793	34.286	17.579	-
c_3	-	-	-	-	-12.404	-	-
d_1	-	-	-	-	-	-	-0.379
$F_R^1(x)$							
a_1	1.240	1.332	-	-	-	-	-
a_2	-2.102	-3.833	-	-	-	-	-
a_3	-	6.228	-	-	-	-	-
b_1	-	-	1.363	1.774	0.996	9.800	-
b_2	-	-	2.816	11.497	27.413	0.801	-
b_3	-	-	-	3.934	0.802	15.753	-
b_4	-	-	-	-	-	48.822	-
c_1	-	-	5.882	20.740	16.773	1.366	-
c_2	-	-	4.267	1.326	58.324	16.228	-
c_3	-	-	-	-	254.194	-	-
d_1	-	-	-	-	-	-	-0.296

Table 1. The fitted parameters of the $F_R(x)$, $F_R^*(x)$, and $F_R^1(x)$ functions.

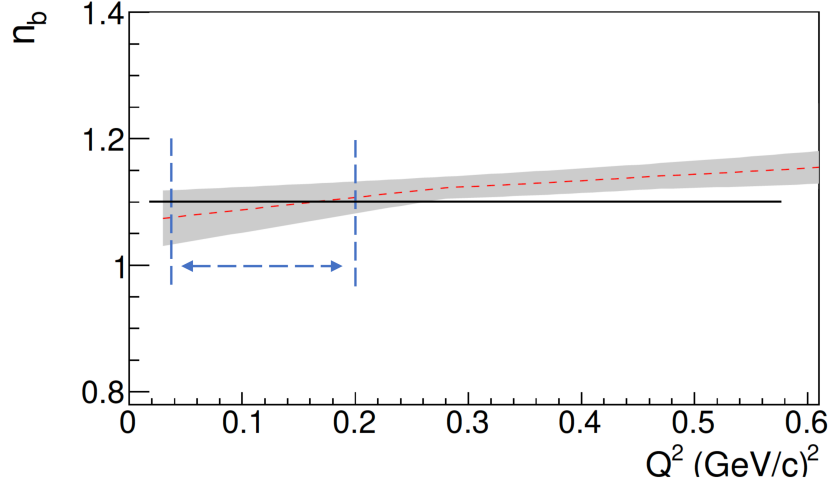


Figure 1. The breaking corrections n_b (dashed line) and δn_b uncertainty (shaded band) at the 1σ or 68% confidence level. The solid line indicates the n_b as theoretically determined in¹². The horizontal double-arrow marks the Q^2 -range where the corrections have been employed for the measurement of G_E^n in this work.

- The procedure is then repeated for all appropriate functions.
- We combine all of the above $n_b(Q^2)$ results (i.e. as derived for all the functional forms) and we experimentally determine the $n_b(Q^2) \pm \delta n_b(Q^2)$: The $n_b(Q^2) = [n_{b(\max)}(Q^2) + n_{b(\min)}(Q^2)]/2$, where $n_{b(\max)}$ and $n_{b(\min)}$ are the maximum and minimum n_b derived at a given Q^2 . The $\delta n_b(Q^2)$ results from the maximum spread of the $n_b(Q^2)$ solutions at any given Q^2 , i.e. $[n_{b(\max)}(Q^2) - n_{b(\min)}(Q^2)]$.

Since the neutron data do not extend lower than $Q^2 = 0.14$ (GeV/c)² we have decided to explore refinements in the determination of n_b by utilizing state of the art LQCD calculations for the G_E^n/G_M^n ratio that extend lower in Q^2 . The LQCD results bring valuable input in describing the Q^2 -dependence of G_E^n/G_M^n in this region based on ab-initio QCD calculations, thus having the potential to drive more accurately the fits. The procedure followed here is the following:

- First, the LQCD G_E^n/G_M^n results are normalized to the neutron world data, within the region where there is overlap for both data sets i.e. $Q^2 \geq 0.14$ (GeV/c)². The LQCD results agree remarkably well to the experimental data but we nevertheless introduce this normalization in order to absolutely baseline the two data sets within the Q^2 range that they overlap.
- The $F_R^1(k)$ is then determined by fitting the LQCD data to the same set of functions, as in the previous step, for the full momentum transfer range of the LQCD data-set so that the data at $Q^2 < 0.14$ (GeV/c)² are included.
- The breaking corrections are now given by: $n_b(k) = F_R^*(k)/F_R^1(k)$

For $Q^2 \geq 0.14$ (GeV/c)² the corrections are naturally identical to the ones determined using the experimental neutron data, since there the LQCD ratios have been normalized to the experimental data. For the lower Q^2 region, the resulting refinement to the n_b determination is $\leq \pm 0.3\%$ i.e. $\delta n_b(Q^2) \leq \pm 0.003$. That is an order of magnitude smaller than the total experimental δn_b uncertainty, that ranges between $\pm 2.5\%$ to $\pm 4\%$ in that region. Furthermore, we do not allow these refinements to reduce the δn_b uncertainty in any way, but only to increase it where the results extend it further than what was determined using the experimental data only. The fitted parameters for the $F_R(x)$, $F_R^*(x)$, and $F_R^1(x)$ are given in Table 1. The experimentally determined $n_b(Q^2)$ is shown in Fig. 1 and the shaded band corresponds to the n_b uncertainty. The solid line marks the n_b as theoretically determined in¹², and one can note the remarkable agreement between the theoretical and the experimental values. The n_b results are also listed in Table 2 for the Q^2 range that they have been used for the G_E^n extraction. The G_E^n results and the breakdown of the uncertainties are given in Table 3.

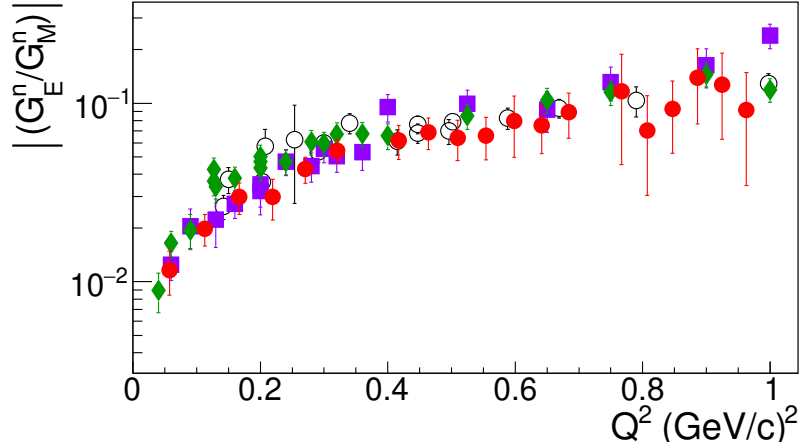


Figure 2. The elastic neutron form factor ratio from the large- N_c analysis.

The G_E^n/G_M^n results from the large- N_c analysis with the Coulomb quadrupole data (filled diamonds) and with the Electric quadrupole data (filled boxes) from measurements^{1-6,18-20}. The neutron world data (open-circles) and the LQCD results (filled circles) are also shown. The error bars correspond to the total uncertainty, at the 1σ or 68% confidence level.

Q^2 (GeV/c) ²	n_b	$n_{b(\min)}$	$n_{b(\max)}$
0.040	1.076	1.034	1.119
0.050	1.078	1.037	1.120
0.060	1.080	1.040	1.120
0.070	1.082	1.043	1.121
0.080	1.084	1.046	1.122
0.090	1.086	1.049	1.123
0.100	1.088	1.052	1.124
0.110	1.090	1.055	1.125
0.120	1.092	1.058	1.125
0.130	1.093	1.061	1.126
0.140	1.095	1.064	1.127
0.150	1.097	1.067	1.128
0.160	1.099	1.070	1.129
0.170	1.101	1.073	1.130
0.180	1.103	1.076	1.131
0.190	1.105	1.079	1.132
0.200	1.107	1.082	1.132

Table 2. The n_b corrections as experimentally determined in the region of the latest G_E^n measurements.

2.2 Analysis within large- N_c

The relation between the G_E^n and the quadrupole transition form factors has also been established through large- N_c relations¹³. The relations take the form

$$\frac{E2}{M1}(Q^2) = \left(\frac{M_N}{M_\Delta}\right)^{3/2} \frac{M_\Delta^2 - M_N^2}{2Q^2} \frac{G_E^n(Q^2)}{F_2^p(Q^2) - F_2^n(Q^2)} \quad (2)$$

$$\frac{C2}{M1}(Q^2) = \left(\frac{M_N}{M_\Delta}\right)^{3/2} \frac{Q_+ Q_-}{2Q^2} \frac{G_E^n(Q^2)}{F_2^p(Q^2) - F_2^n(Q^2)} \quad (3)$$

where $F_2^{p(n)}$ are nucleon's Pauli form factors, M_Δ is the mass of the Δ , and $Q_\pm = ((M_\Delta \pm M_N)^2 + Q^2)^{1/2}$. Here the experimental data base is extended to include the Electric quadrupole (E2) transition, which in turn allows for an improved extraction of the

$Q^2(\text{GeV}/c)^2$	G_E^n	$\delta G_{E(\text{exp})}^n$	$\delta G_{E(\text{mod})}^n$	$\delta G_{E(n_b)}^n$
0.040	0.0128	0.0011	0.0034	0.0005
0.060	0.0222	0.0015	0.0014	0.0008
0.090	0.0242	0.0014	0.0055	0.0008
0.127	0.0420	0.0049	0.0024	0.0013
0.130	0.0388	0.0015	0.0065	0.0012
0.200	0.0460	0.0025	0.0027	0.0010
0.200	0.0397	0.0090	-	0.0009

Table 3. The neutron electric form factor derived within the SU(6) analysis. The G_E^n results with their experimental and model uncertainties, as described in the text (with the uncertainty δn_b constrained by the experimental form factor world data). The last data point, at $Q^2 = 0.20 (\text{GeV}/c)^2$, involves the measurement from $p(e, e' p)\gamma^5$ and it thus does not have a model uncertainty associated with the pion electroproduction background amplitudes.

$Q^2(\text{GeV}/c)^2$	G_E^n	$\delta G_{E(\text{exp})}^n$	$\delta G_{E(\text{th})_1}^n$
0.040	0.0151	0.0010	0.0023
0.060	0.0246	0.0011	0.0037
0.090	0.0285	0.0012	0.0043
0.127	0.0489	0.0040	0.0073
0.130	0.0447	0.0013	0.0067
0.200	0.0525	0.0021	0.0079
0.200	0.0459	0.0074	0.0069

Table 4. The neutron electric form factor derived from the large- N_c analysis. The neutron electric form factor derived from the large- N_c analysis of the Electric and the Coulomb quadrupole amplitude measurements.

G_E^n . For the well known G_E^p , G_M^p and G_M^n , that enter in the expressions through the Pauli form factors, we have used recent parametrizations (see next sections for details).

The above relations come with a 15% theoretical uncertainty¹³ that has been accounted for in the G_E^n extraction. That level of uncertainty is further supported by a third relation, also derived in the same work, that connects the isovector Pauli FF to the $N \rightarrow \Delta$ magnetic dipole FF¹³; that relation has been shown to work well at the 13% level. The level of theoretical uncertainty can be further cross checked using experimental data, when one extracts the G_E^n independently through the Coulomb and the Electric quadrupole transitions. The results from the two different analyses validate the 15% level of agreement, as can be seen in Fig. 2. We have thus adopted this number as a theoretical uncertainty in the data analysis.

From each experiment we derive one G_E^n value, from both the measurements of the Coulomb and of the Electric quadrupole form factor by taking the weighted average of the two independently derived G_E^n values. The results are given in Table 4. The results are in great agreement with that of the SU(6) analysis. The weighted average of the large- N_c and of the SU(6) results leads to the final G_E^n value. The variance of the two values is assigned as a G_E^n theoretical uncertainty, and is accounted for accordingly in the r_n extraction. The final results for G_E^n are given in Table 5.

$Q^2(\text{GeV}/c)^2$	G_E^n	δG_E^n	$\delta G_{E(\text{th})_2}^n$
0.040	0.0143	0.0020	0.0012
0.060	0.0228	0.0019	0.0012
0.090	0.0269	0.0035	0.0021
0.127	0.0442	0.0047	0.0034
0.130	0.0417	0.0048	0.0030
0.200	0.0471	0.0035	0.0033
0.200	0.0425	0.0067	0.0031

Table 5. Final results for the neutron electric form factor. The G_E^n final results as derived from the SU(6) and the large- N_c analysis. The theoretical uncertainty is derived from the variance of the results from the two analyses.

3 Neutron charge radius extraction

The neutron mean square charge radius is related to the slope of the neutron electric form factor as $Q^2 \rightarrow 0$ through

$$\langle r_n^2 \rangle = -6 \frac{dG_E^n(Q^2)}{dQ^2} \Big|_{Q^2 \rightarrow 0}. \quad (4)$$

The $G_E^n(Q^2)$ has to be parametrized and fitted to the experimental data, and from the slope at $Q^2 = 0$ the $\langle r_n^2 \rangle$ is determined. The data derived in this work offer the level of precision, and the Q^2 -range, that allow to explore for suitable $G_E^n(Q^2)$ functional forms with an additional free parameter compared to what was possible in the past (i.e. with three free parameters). In turn, this allows to extract the $\langle r_n^2 \rangle$ from the G_E^n measurements, which has not done before. We have explored various functional forms in order to identify those appropriate, in the following way:

- i) The functions have been fitted to the G_E^n results reported in this work (data-set in Table 5) and to the world data^{14,15,21–32}.
- ii) For the functions that offer a good fit to the data, further tests are performed with pseudo-data; these tests aim to place the parametrizations under stress in terms of their limitations to fits that engage data of higher precision and of extended kinematical coverage.
- iii) The $\langle r_n^2 \rangle$ extraction is repeated with multiple G_M^n parametrizations so that the uncertainty introduced by the G_M^n parametrization is quantified; for that part we have found ± 0.0009 (fm²), an order of magnitude smaller compared to the total $\langle r_n^2 \rangle$ uncertainty.

Our studies have shown that the most robust function for the radius extraction takes the form

$$G_E^n(Q^2) = (1 + Q^2/A)^{-2} \frac{B\tau}{1 + C\tau}, \quad (5)$$

where $\tau = Q^2/4m^2$, and A, B, C are free parameters. It involves a similar form to the Galster³³. The Galster is a long standing phenomenological parametrization that could adequately describe the early G_E^n data, but as recent experiments revealed^{34,2} it does not have sufficient freedom to accommodate reasonable values of the radius, without constraining or compromising the fit (note: the reference Phys. Rev. C83, 055203 (2011) was inadvertently not included in the version of the paper that was submitted at Nature Communications). Here, instead of using the standard dipole form factor with $\Lambda^2 = 0.71(\text{GeV}/c)^2$ an additional free parameter A is introduced (see Eq. 5). Our fit to the data gives $\langle r_n^2 \rangle = -0.110 \pm 0.008$ (fm²) with a reduced χ^2 of 0.74. The fitted parameters are given in Table 6.

A second parametrization, giving a good fit to the data, involves the sum of two dipoles

$$G_E^n(Q^2) = \frac{A}{(1 + \frac{Q^2}{B})^2} - \frac{A}{(1 + \frac{Q^2}{C})^2}. \quad (6)$$

This form has been explored in the past^{15,34} with three free parameters and with the $\langle r_n^2 \rangle$ already constrained by the measurement of the neutron-electron scattering length. This fit (see Table 6) exhibits an excellent agreement to the one of Eq. 5. The two curves are nearly indistinguishable by eye as seen in Fig. 3a. Considering the weighted average of the two methods we derive a nearly identical result of $\langle r_n^2 \rangle = -0.110 \pm 0.007$ (fm²). Nevertheless, our pseudo-data studies showed that the two-dipole fit suffers from limitations in the determination of the G_E^n -slope. We thus adopt only the parametrization of Eq. 5 and quote its fitted result $\langle r_n^2 \rangle = -0.110 \pm 0.008$ (fm²) as our final result for the neutron charge radius.

Parametrization	A	B	C
Param. 5	0.505 ± 0.079	1.655 ± 0.126	0.909 ± 0.583
Param. 6	0.130 ± 0.039	1.790 ± 0.409	0.419 ± 0.0980

Table 6. Fitted parameters for the two G_E^n parametrizations.

We have also explored the radius extraction by adopting the scenario where the uncertainty of the symmetry breaking corrections in the SU(6) analysis is treated very conservatively i.e. $n_b = 1.1 \pm 0.1$. In this case the final result becomes $\langle r_n^2 \rangle = -0.109 \pm 0.009$ (fm²) with a reduced χ^2 of 0.74. This scenario tends to overestimate the uncertainty of the symmetry breaking terms, but as this is not a dominant factor in the radius extraction the r_n -uncertainty is not affected significantly.

The particle data group (PDG) average value, $\langle r_n^2 \rangle = -0.1161 \pm 0.0022$ (fm²), is the weighted average of five values^{35–38} based on the measurement of the neutron-electron scattering length. One of these measurements³⁷ disagrees with^{35,36}, but as this disagreement has not been resolved the value from measurement³⁷ is considered in the PDG average, for the time being.

²The reference Phys. Rev. C83, 055203 (2011) was inadvertently not included in the version of the paper that was submitted at Nature Communications

Our result, $\langle r_n^2 \rangle = -0.110 \pm 0.008 \text{ (fm}^2\text{)}$, comes to update the world average value for the neutron charge radius. The recent measurement, like the ones from^{35,36}, also disagrees with that of³⁷, and considering that this disagreement comes from a different method for the radius extraction one may want to exclude the value of³⁷ from the world data average. The latest weighted average value, including our measurement and excluding the one of³⁷, becomes $\langle r_n^2 \rangle = -0.1152 \pm 0.0017 \text{ (fm}^2\text{)}$ and is shown in Fig. 3b. In the current PDG world-data average, the uncertainty that is calculated following the standard weighted least-squares procedure is further enhanced by a factor of $S = [\chi^2/(N-1)]^{1/2}$ due to the discrepancies that are introduced from the inclusion of the Alexandrov'86 measurement in the data-set. In the most recent world-data average, with the inclusion of the new measurement and the subsequent exclusion of the Alexandrov'86, these discrepancies are raised and the term S does not contribute any further to the world-data average uncertainty. Effectively, the biggest benefit to the uncertainty results from the resolution of the discrepancies in the $\langle r_n^2 \rangle$ measurements that the current work allows for. For the completeness of this discussion, we can also comment that if one considers in the world-data average both the new $\langle r_n^2 \rangle$ measurement as well as that of Alexandrov'86, then the uncertainty improves by 10%, from $\pm 0.0022 \text{ (fm}^2\text{)}$ to $\pm 0.0020 \text{ (fm}^2\text{)}$. Nevertheless, the results of this work suggest that the Alexandrov'86 has to be eliminated from the world-data average in which case the uncertainty is further reduced to $\pm 0.0017 \text{ (fm}^2\text{)}$.

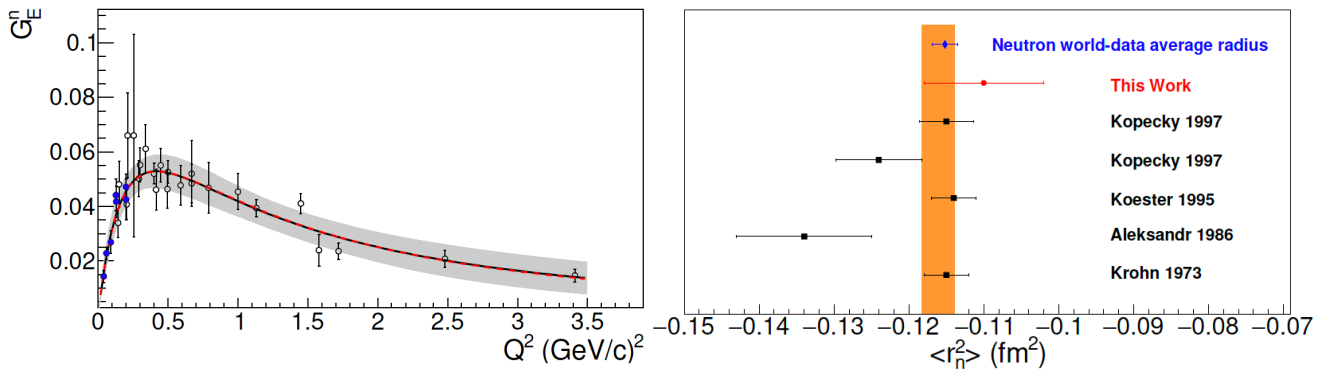


Figure 3. Left panel: The G_E^n results from this work (filled-circles) and the G_E^n world data (open-circles)^{14,15,21–32}. The error bars correspond to the total uncertainty, at the 1σ or 68% confidence level. The solid (black) curve shows the fit to the data from the parametrization of Eq. 5 with its uncertainty (shaded band). The dashed (red) line shows the fit from parametrization of Eq. 6. The two fits practically overlap. Right panel: The $\langle r_n^2 \rangle$ measurement from this work and from the references^{35–38} that are currently included in the PDG $\langle r_n^2 \rangle$ analysis. The orange-band marks the PDG averaged $\langle r_n^2 \rangle$ value. The recent weighted average of the world data is also shown, when the $\langle r_n^2 \rangle$ measurement reported here is included in the calculation.

3.1 Extraction from fits within a limited low- Q^2 range

The extraction of the neutron charge radius has been performed by fitting over an extended Q^2 range, following the experience from the extraction of the proton charge radius, where the world data base is far more extensive compared to the one of the neutron. In that case, the charge radius extraction has been traditionally based on fits of functional forms over an extended kinematic Q^2 range (e.g. such as in the most recent r_p extraction from the Mainz G_E^p measurements, etc). Fitting over a limited low Q^2 -range in order to extract the proton radius was first attempted very recently, at the PRad experiment. In that case though the G_E^p was accessed at much lower momentum transfers compared to the neutron measurements, namely in the range $Q^2 = 0.0002 \text{ (GeV/c)}^2$ to $Q^2 = 0.06 \text{ (GeV/c)}^2$.

One consideration here is that the proton and the neutron electric form factor parametrizations are inherently different (i.e. the G_E^n changes slope and follows a monotonic fall-off at low Q^2). With that in mind we here explore the potential of G_E^n fits that are limited only in the low Q^2 region. The global fit for G_E^n shows that a maximum is reached shortly after $Q^2 = 0.4 \text{ (GeV/c)}^2$. We thus limit our studies within the range $[0 - 0.4 \text{ (GeV/c)}^2]$ that G_E^n is expected to be monotonic. In doing so one has to consider to following factors: what is the choice of the functional forms and the number of parameters that will be fitted, what is the optimal fitting range, and how does the extracted radius depend on the ansatz for the fit model. Here we follow a procedure that has been frequently adopted for the extraction of the proton charge radius. We have studied a variety of functions so that we can identify those that are appropriate for the fit to the data. The functional forms that allow the extraction of the charge radius with a meaningful precision are divided in two groups. The first group is based on polynomials and involves polynomials with varying orders and combinations of polynomials with a dipole. The stability of the extracted radius is observed within the group by using polynomials of different degree, while the variance of the fitted values indicates the model uncertainty of the

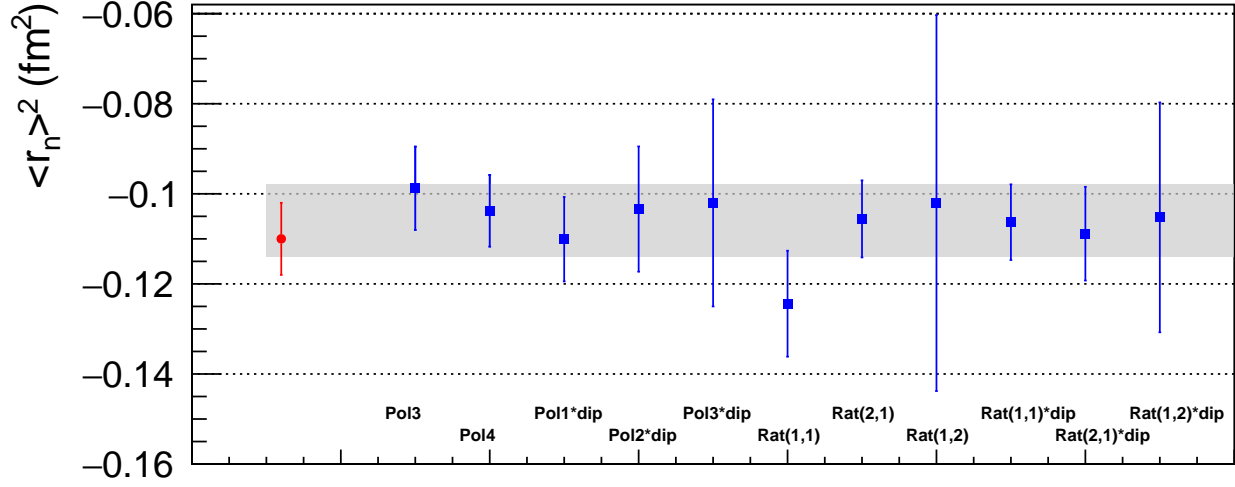


Figure 4. The $\langle r_n^2 \rangle$ as extracted with the different model functions (blue boxes) from fits within the low Q^2 range. The error bars correspond to the total uncertainty, at the 1σ or 68% confidence level. The gray band marks the final result, from the combination of all the fits of both groups of functions (see text for details as well as Tab. 7). The red point marks the final result from the fit over the extended Q^2 range, namely $\langle r_n^2 \rangle = -0.110 \pm 0.008$ (fm²).

group. The second group is based on rational functions of the form

$$\text{Rat}(i, j)(Q^2) = \frac{\sum_{i=1}^n \alpha_i Q^{2i}}{1 + \sum_{j=1}^m \beta_j Q^{2j}}$$

and combinations of Rat(n,j) with dipole. These groups of functions have been utilized in the past for the proton radius extraction. Other functional forms that we explored (e.g. exponential-based functions $f(Q^2) = \sum_{i=0}^n \alpha_i Q^{2i} (1 - e^{-\beta Q^2})$, etc) give consistent results for the charge radius but with large uncertainties and as such we do not consider them here. When it comes to the number of fitted parameters, n_p , one has to make sure that n_p is not too small since in such a case the data will not be properly reproduced, while at the same time one has to avoid a very high level of flexibility in order to avoid erratic fits. For example, in the polynomial fits we have found that starting with a 3rd order polynomial we can have a good fit, but after the 5th order polynomial the fitted function follows an erratic, non-monotonic behavior through the data points at the higher end of the Q^2 fitting range. In the latter case, the fitted value for the $\langle r_n^2 \rangle$ is found to be consistent to that of the fits with the lower order polynomials. Nevertheless, for consistency we have decided to exclude such fits from the determination of the charge radius since our requirement is to fit a monotonic function at low momentum transfers. Polynomials \times dipole were able to provide a good fit, contrary to polynomial+dipole that would result into non-stable, erratic fits. Functional forms within the group were not considered when their resulting uncertainties were too large to contribute meaningfully to the determination of the charge radius, such as rational functions higher than Rat(2,2). The $\langle r_n^2 \rangle$ results from the individual fits within the two groups are shown in Fig. 4. The comparison of all the G_E^n fits for the functions within the two groups are shown in Fig. 5.

	[0 - 0.3 (GeV/c) ²]	[0 - 0.4 (GeV/c) ²]
Polynomial group	$\langle r_n^2 \rangle = -0.105 \pm 0.006 \pm 0.002_{\text{mod}}$ (fm ²)	$\langle r_n^2 \rangle = -0.104 \pm 0.005 \pm 0.003_{\text{mod}}$ (fm ²)
Rational group	$\langle r_n^2 \rangle = -0.108 \pm 0.006 \pm 0.002_{\text{mod}}$ (fm ²)	$\langle r_n^2 \rangle = -0.108 \pm 0.006 \pm 0.002_{\text{mod}}$ (fm ²)
	$\langle r_n^2 \rangle = -0.107 \pm 0.006 \pm 0.002_{\text{mod}} \pm 0.002_{\text{group}}$ (fm ²)	

Table 7. The extracted $\langle r_n^2 \rangle$ from the fits within a low- Q^2 range.

For the charge radius, the weighted average is extracted separately for each one of the two groups. A systematic uncertainty

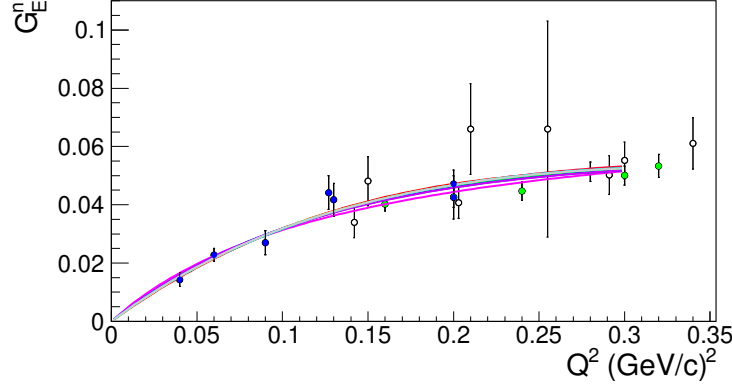


Figure 5. The low- Q^2 G_E^n fits with all the functions within the polynomial and the rational groups. The data from the analysis of the MAMI and Hall-A measurements are marked as blue points and the ones from the CLAS as green points. The error bars correspond to the total uncertainty, at the 1σ or 68% confidence level.

is also quantified within each group (i.e. a model uncertainty of the group) from the weighted variance of the results from all the fits within the group. The results from the two groups tend to have a similar total uncertainty (i.e. when the weighted average and the group's model uncertainty are combined). Nevertheless there is a small systematic difference of the two group's central values, as studies over a varying fitting range have shown. For that reason a third uncertainty is determined: here we consider the spread of the two central values as indicative of the uncertainty that is associated with the choice of the group. Therefore the final result is given by the average of these two values, while the half of the difference of the two values is assigned as an additional (group) uncertainty (see Tab. 7). This uncertainty has to be added linearly, and not quadratically, to the other two uncertainties. Lastly, the sensitivity of the results to the fitting range has been explored. There is an interplay of the fitting and of the model/group uncertainties depending on the fitting range in Q^2 . Our studies have shown that as we increase the upper bound of the fitting range, Q_{\max}^2 , the fitting uncertainties tend to improve but at the expense of the group's model uncertainty. When all uncertainties are considered, the overall level of uncertainty for the results within the $[0 - 0.3 \text{ (GeV/c)}^2]$ and within the $[0 - 0.4 \text{ (GeV/c)}^2]$ range are comparable, with a very small benefit if the fits are conducted within the $[0 - 0.3 \text{ (GeV/c)}^2]$. As a general remark, when the overall uncertainty (i.e. from the combination of the fitting and model ones) is equivalent for two different fitting ranges it may be preferable to pursue the results through fits within the range where the model uncertainties tend to minimize, considering that the fitting uncertainties are very strictly defined and accurately determined, while the determination of model uncertainties entails a higher level of uncertainty. Lastly, limiting the fitting range even further, within the $[0 - 0.2 \text{ (GeV/c)}^2]$ range, is not beneficial since the fitting uncertainties increase significantly. The results from the fits within each group are shown in Tab. 7. With the low- Q^2 fits we find that $\langle r_n^2 \rangle = -0.107 \pm 0.006 \pm 0.002_{\text{mod}} \pm 0.002_{\text{group}} \text{ (fm}^2\text{)}$. This value is in excellent agreement compared to what we derive when we fit within the extended Q^2 range, namely $\langle r_n^2 \rangle = -0.110 \pm 0.008 \text{ (fm}^2\text{)}$. Nevertheless we conclude that the fits at low- Q^2 are not able to provide a more precise determination of $\langle r_n^2 \rangle$ compared to the fit over the extended Q^2 range, while a higher level of model uncertainty is introduced to the result by the low- Q^2 fits. We here note that the inclusion of the CLAS data in the low- Q^2 fits (see Section 3.2 that follows) reveal a further increase to the *group* uncertainty, from $\pm 0.002_{\text{group}} \text{ (fm}^2\text{)}$ to $\pm 0.004_{\text{group}} \text{ (fm}^2\text{)}$. Our studies indicate that more data are required lower in Q^2 so that these uncertainties can be further suppressed, and that the G_E^n fits over the extended Q^2 range provide the most precise and consistent measurement of $\langle r_n^2 \rangle$.

3.2 Extraction including additional data at higher Q^2

The limiting factor in the extraction of the neutron charge radius has been the lack of G_E^n data at low momentum transfers. This limitation is now raised by the latest data provided by the MAMI and the JLab/Hall-A measurements in the region $Q^2 = 0.04 \text{ (GeV/c)}^2$ to $Q^2 = 0.20 \text{ (GeV/c)}^2$. The intermediate and the high Q^2 regime on the other hand is already sufficiently covered by the G_E^n world data and the $\langle r_n^2 \rangle$ fits are not limited by the lack of data in this region.

The quadrupole transition form factor measurements extend higher in Q^2 , in the region that has already been accessed by G_E^n measurements. One can thus naturally consider to extend the current analysis to higher momentum transfers so as to enrich the G_E^n data base even further, with overlapping measurements, in the hope to improve the fits for the $\langle r_n^2 \rangle$ extraction. In principle one can attempt to do that. Nevertheless, while the relations that relate the G_E^n to the quadrupole transition form factors hold on very solid ground in the low Q^2 region (i.e. the region of the MAMI and the JLab/Hall-A measurements) they tend to hold less well at high momentum transfers. There is no sharp, formally defined Q^2 cut-off-value after which these

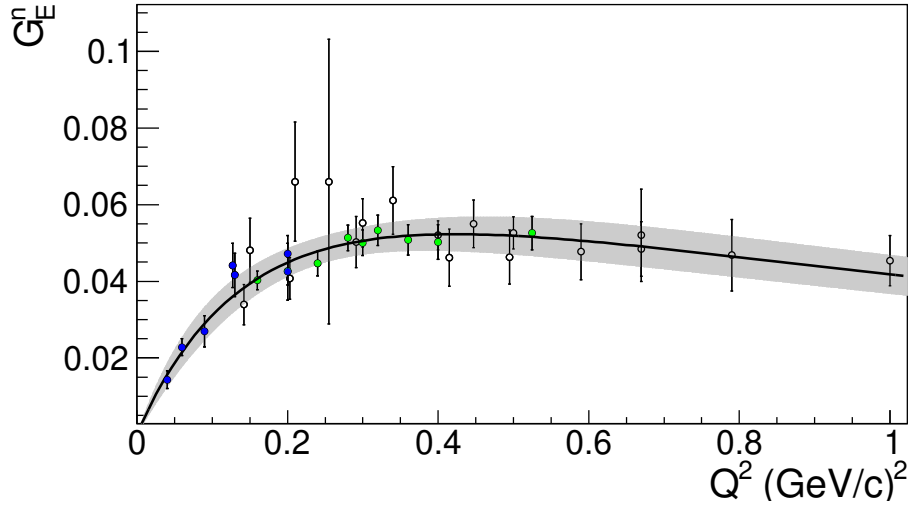


Figure 6. The G_E^n results from the MAMI and the JLab/Hall-A measurements (blue points) and from the CLAS measurements (green points). The error bars correspond to the total uncertainty, at the 1σ or 68% confidence level.

relations do not hold, and as such they should be treated with caution at increasing momentum transfers e.g. their level of theoretical uncertainty tend to increase around $\approx 1 \text{ (GeV/c)}^2$ to a level that one may not wish to risk including them in the current analysis, considering the level of precision that we are after for the charge radius extraction. One thus has to walk along a fine line, by adding measurements at intermediate momentum transfers, e.g. higher than $Q^2 = 0.20 \text{ (GeV/c)}^2$ but not going very high in Q^2 , so that a clear benefit to the r_n extraction is achieved and without compromising the extraction with theoretical uncertainties.

Here we expand the range of our analysis and we extract the G_E^n from the JLab/CLAS⁶ lowest momentum-transfer data-set which involves measurements of the quadrupole transition form factors up to $Q^2 = 0.52 \text{ (GeV/c)}^2$. The measurements are taken within a kinematic region where one can still feel comfortable applying these relations. The extracted G_E^n from these measurements is shown in Fig. 6, and the results are in excellent agreement with the G_E^n world data in the same region. When we include this additional set of data in the $\langle r_n^2 \rangle$ extraction and we fit over the complete Q^2 -range of the G_E^n measurements we find a $\langle r_n^2 \rangle = -0.107 \pm 0.007 \text{ (fm}^2\text{)}$, compared to $\langle r_n^2 \rangle = -0.110 \pm 0.008 \text{ (fm}^2\text{)}$ when the CLAS data are not included. Here we observe a minor improvement to the $\langle r_n^2 \rangle$ uncertainty with the inclusion of the CLAS data, but we suggest that this result is treated with some caution. We have some concerns, that part of the reported CLAS uncertainties may be underestimated which could in turn influence / bias the level of the $\langle r_n^2 \rangle$ uncertainty. We discuss these considerations in more detail in the section that follows (Section 3.2.1).

We do not consider extending the data-set with measurements at higher Q^2 e.g. by including the CLAS data that are higher than $Q^2 \approx 0.7 \text{ (GeV/c)}^2$, for the following reasons. Firstly, as we noted above, in such a case we would be entering a region that is associated with a high level of theoretical uncertainties. Secondly, when we investigate the effect of including the additional data up to $Q^2 = 1 \text{ (GeV/c)}^2$ we did not observe any further benefit to the fits, namely we derive the same level of $\langle r_n^2 \rangle$ uncertainty. Thus in such a case one would risk to introduce further uncertainties of theoretical nature to the $\langle r_n^2 \rangle$ extraction without any benefit to the fitting uncertainty. Lastly, the CLAS results at $Q^2 = 1 \text{ (GeV/c)}^2$ disagree with the results from the Hall-A experiment²⁰ at the same Q^2 that is based on recoil polarization measurements. The Hall-A experiment offers a nearly model-independent analysis and also utilizes a setup with superior resolution compared to the one of CLAS. If we were to consider these (disagreeing) data we could risk further bias to the $\langle r_n^2 \rangle$ extraction from the tensions among the competing transition form factors measurements in that region.

Lastly, we explore the influence of the CLAS data to the $\langle r_n^2 \rangle$ extraction from the fits within a limited low- Q^2 range, as discussed in Section 3.1. The results for the fitted functions when the CLAS data are included are shown in Fig. 7 and they are compared to the results of the fits when the CLAS data are not included in the analysis. The final results are summarized in Tab. 8. Looking at the results we are able to make a number observations and to draw a set of conclusions with regard to the strength of the low- Q^2 fits. First, we note that the results of the polynomial group maintains remarkable stability compared to the analysis when the CLAS data are not included. The central value of the rational group, on the other hand, observes a shift compared to the analysis when the CLAS data are not included. This effectively enhances the group uncertainty from

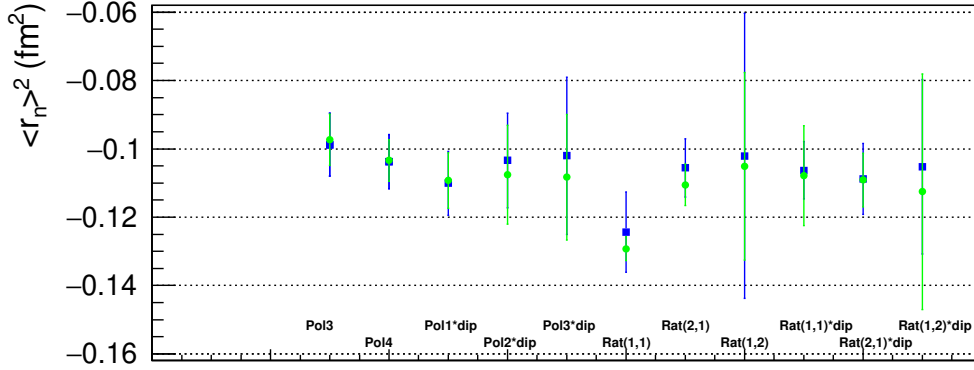


Figure 7. The $\langle r_n^2 \rangle$ as extracted with the different model functions from fits within the low Q^2 range. The results are shown with the inclusion of the CLAS data (green circles) and without (blue boxes). The error bars correspond to the total uncertainty, at the 1σ or 68% confidence level.

$\pm 0.002_{\text{group}}$ (fm²) to $\pm 0.004_{\text{group}}$ (fm²) when the CLAS data are included. Another observation is that the model uncertainty within each group tends to also increase when we fit in the $[0 - 0.4 \text{ (GeV}/c)^2]$ range, but not at the $[0 - 0.3 \text{ (GeV}/c)^2]$ range. One can conclude that for low- Q^2 fits within that region we are rather sensitive to model uncertainties that depend on the choice of the fitted parametrization. These uncertainties tend to be comparable to the statistical uncertainty of the fits. These uncertainties can be further suppressed when more data are acquired at lower momentum transfers and the fitting range can be limited even lower in Q^2 .

	$[0 - 0.3 \text{ (GeV}/c)^2]$	$[0 - 0.4 \text{ (GeV}/c)^2]$
Polynomial group	$\langle r_n^2 \rangle = -0.107 \pm 0.006 \pm 0.001_{\text{mod}}$ (fm ²)	$\langle r_n^2 \rangle = -0.104 \pm 0.004 \pm 0.004_{\text{mod}}$ (fm ²)
Rational group	$\langle r_n^2 \rangle = -0.115 \pm 0.006 \pm 0.002_{\text{mod}}$ (fm ²)	$\langle r_n^2 \rangle = -0.115 \pm 0.005 \pm 0.007_{\text{mod}}$ (fm ²)
	$\langle r_n^2 \rangle = -0.111 \pm 0.006 \pm 0.002_{\text{mod}} \pm 0.004_{\text{group}}$ (fm ²)	

Table 8. The extracted $\langle r_n^2 \rangle$ from the fits within a low- Q^2 range when the CLAS measurements are included in the data-set. The final result, from the average of the two groups, is given for the fits in the $[0 - 0.3 \text{ (GeV}/c)^2]$ range, where the model uncertainties are minimized.

3.2.1 Considerations on the CLAS data uncertainties

The CLAS results agree nicely with the MAMI and JLab/Hall-A measurements within their region of overlap at $Q^2 \approx 0.2 \text{ (GeV}/c)^2$. Nevertheless, we have some concerns that part of the CLAS uncertainties may be underestimated. If that is indeed the case, one could risk to bias the $\langle r_n^2 \rangle$ extraction when these data are included in the analysis. More specifically, the CLAS detector has a large acceptance coverage (4π), which offers some advantage as to the extent of the measured phase space. Nevertheless, this advantage comes at the expense of the detector's resolution, when compared to the high resolution spectrometers that have been utilized for the MAMI and the JLab/Hall-A measurements. In the latter case (i.e. at MAMI and in Hall-A) the extended phase space is still covered by sequential measurements of the high resolution spectrometers so that one can ultimately achieve an extended phase space coverage that is comparable to the CLAS one. Thus one would naturally expect that ultimately the MAMI and the JLab/Hall-A results will offer smaller overall experimental uncertainties in the transition form factor extraction since e.g. the expectation is that the limitations in the resolution of CLAS will introduce a higher level of systematic uncertainties in the CLAS results. But this is not what one observes in the reported results. The CLAS measurements are reported with superior experimental uncertainties (compared to the MAMI and the Hall-A data). This points out to a potential underestimation for part of the experimental uncertainties within the global fit analysis of the extended CLAS 4π acceptance. We here note that the extraction of the quadrupole transition amplitudes involves a very delicate task since it requires to isolate and extract a very small amplitude from multiple interfering background processes of similar magnitude. A second concern involves the level of the model uncertainties of the CLAS data. One would naturally expect that these uncertainties are not very much dependent on the experimental setup, and that they will be approximately at the same

α_1	α_2	b_1	b_2	b_3	b_4
0.13830 ± 0.12960	0.00011 ± 0.00093	11.1944 ± 0.14021	19.6659 ± 1.1020	30.5455 ± 5.45231	2.35740 ± 0.03289

Table 9. The G_E^p fitted parameters.

level for all data sets (CLAS, Hall-A, MAMI) at the same kinematics. Nevertheless, the reported CLAS model uncertainties are nearly a factor of two smaller compared to the ones of MAMI and Hall-A. One can note here that in the CLAS analysis only two theoretical models have been utilized for the quantification of the model uncertainties, while for the MAMI and Hall-A data a more complete study that engages four theoretical models, as well as an experimental measurement of the photon excitation channel has been considered (as described in detail in earlier sections of this document). Taking the above considerations into account one may wonder if the small improvement that we observe in the r_n uncertainty by the inclusion of the CLAS data, in a region where G_E^n data already exist, is affected by a potential underestimation of these uncertainties. In any case, and for the completeness of this work, we report the results for the $\langle r_n^2 \rangle$ extraction when the CLAS data are included in the analysis, but we suggest that this result is considered with a level of reservation.

4 Flavor dependent charge densities

The neutron and the proton charge densities³⁹ can be extracted in the infinite-momentum-frame through:

$$\rho(b) = \int_0^\infty \frac{dQ}{2\pi} Q J_0(Qb) \frac{G_E(Q^2) + \tau G_M(Q^2)}{1 + \tau} \quad (7)$$

where b is the transverse distance, $\tau = Q^2/4m^2$ and J_0 a cylindrical Bessel function. From the neutron and proton densities, invoking charge symmetry, and neglecting the $s\bar{s}$ contribution, we then extract the u - and d -quark densities, where

$$\rho_u(b) = \rho_p(b) + \rho_n(b)/2 \quad \rho_d(b) = \rho_p(b) + 2\rho_n(b). \quad (8)$$

Here we utilize the most recent parametrizations of the nucleon form factors. For the neutron electric form factor we use the parametrization determined in this work i.e. the one of Eq. 5 (Table 6). For the two magnetic form factors, G_M^p and G_M^n , we use¹⁶. For G_E^p we have performed an updated parametrization for the following reasons: i) so that we may include important and recent measurements from⁴⁰ that were not yet available in¹⁶, and ii) so that we may eliminate a constraint on the proton charge radius that has been enforced in¹⁶, which is not in agreement with recent measurements of the proton charge radius. Here we have used a form that has been widely adopted in the past:

$$G_E^p = \frac{1 + \left(\sum_{i=1}^2 a_i x_i^i \right)}{\left(1 + \sum_{j=1}^4 b_j x_j^j \right)} \quad (9)$$

The G_E^p fitted parameters that we have derived are given in Table 9.

The extracted neutron (ρ_n), proton (ρ_p) are presented in Fig. 8. The u - and d -quark densities with their experimental uncertainties are shown at Fig. 5c in the paper. The uncertainties in the charge density distributions result from the uncertainties of the nucleon form factor parametrizations, as they have been determined from the fits of the experimental data. Our data, being particularly sensitive to neutrons long distance structure, offer a factor of 2 improvement in the precision of the neutron charge density at its surface as seen in Fig. 9.

5 Lattice QCD results

To extract the lattice data presented in this work, we utilize results from a recent calculation by the Extended Twisted Mass Collaboration (ETMC) on the electromagnetic form factors of the proton and neutron⁴¹. The lattice calculation is pioneering in more than one ways. First, the numerical simulations have been performed taking into account the up, down, strange and charm quark in the sea ($N_f = 2 + 1 + 1$ of twisted mass clover-improved fermions). All of the quark masses are fixed to their physical value (physical point), reproducing a pion mass of 139 MeV. In addition, the ensemble has volume with spatial extent 5.12 fm, and a lattice spacing $a = 0.08$ fm. Having a lattice spacing below 0.1 fm, and a large volume, significantly suppressed finite-volume effects and discretizations effects.

Beyond the state-of-the-art ensemble used for the calculation of the electromagnetic form factors, several sources of systematic uncertainties are controlled. Dominance of ground state is reliably established by three methods to analyze the data:

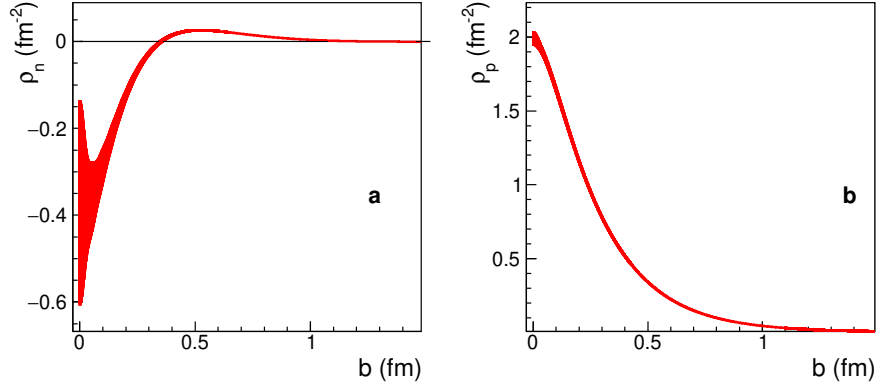


Figure 8. The neutron charge density (panel a) and the proton charge density (panel b).

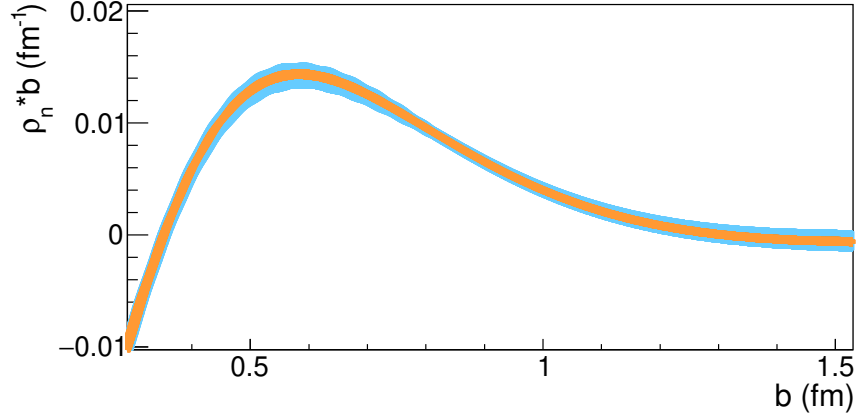


Figure 9. The neutron charge density at it's surface, as derived with (without) our G_E^n data is shown by the inner (outer) band.

single-state fit, two-state fit, and the so-called summation method^{42,43}. Furthermore, both the connected and disconnected contributions are included to extract the proton and neutron electromagnetic form factors at the physical point. The achieved accuracy for both connected and disconnected contributions is very high, which is a very challenging task for simulations at the physical point. In fact, it is also shown that the disconnected contributions are non-negligible, reaching up to 15%. Along the same lines, the strange quark contribution to the electromagnetic form factors has been calculated⁴⁴, which is, however, beyond the scope of this work.

Here we used the aforementioned data to extract the ratio between the neutron electric and magnetic form factor (G_E^n/G_M^n). The results are shown in Table 10. The very good agreement of the results with the experimental data indicates that lattice QCD has advanced significantly, leading to results of high reliability. The errors include both statistical and systematic uncertainties added in quadrature. For the ratios we perform a jackknife statistical-error analysis, and an error propagation analysis using the individual data on G_E^n and G_M^n . The resulting mean values and errors are almost identical between the two methods.

$Q^2(\text{GeV}/c)^2$	$\frac{G_E^n}{G_M^n}$	$\delta(\frac{G_E^n}{G_M^n})$
0.057	0.0116	0.0032
0.113	0.0198	0.0040
0.167	0.0298	0.0060
0.219	0.0298	0.0077
0.271	0.0427	0.0071
0.321	0.0543	0.0084
0.417	0.0618	0.0134
0.464	0.0688	0.0137
0.510	0.0639	0.0162
0.554	0.0658	0.0176
0.598	0.0797	0.0300
0.642	0.0751	0.0228
0.684	0.0889	0.0251
0.767	0.1167	0.0715
0.807	0.0702	0.0397
0.847	0.0928	0.0403
0.886	0.1392	0.0626
0.925	0.1267	0.0638
0.963	0.0916	0.0571

Table 10. Lattice results for $\frac{G_E^n}{G_M^n}$.

References

1. Blomberg, A. *et al.* Electroexcitation of the $\Delta^+(1232)$ at low momentum transfer. *Phys. Lett.* **B760**, 267–272 (2016).
2. Stave, S. *et al.* Lowest Q^2 Measurement of the $\gamma^* p \rightarrow \Delta$ Reaction: Probing the Pionic Contribution. *Eur. Phys. J.* **A30**, 471–476 (2006).
3. Sparveris, N. *et al.* Measurements of the $\gamma^* p \rightarrow \Delta$ reaction at low Q^2 . *Eur. Phys. J.* **A49**, 136 (2013).
4. Sparveris, N. F. *et al.* Determination of quadrupole strengths in the $\gamma^* p \rightarrow \Delta(1232)$ transition at $Q^2 = 0.20 (\text{GeV}/c)^2$. *Phys. Lett.* **B651**, 102–107 (2007).
5. Blomberg, A. *et al.* Virtual Compton Scattering measurements in the nucleon resonance region. *Eur. Phys. J. A* **55**, 182 (2019). [1901.08951](#).
6. Aznauryan, I. G. *et al.* Electroexcitation of nucleon resonances from CLAS data on single pion electroproduction. *Phys. Rev.* **C80**, 055203 (2009).
7. Kamalov, S. & Yang, S. N. Pion cloud and the Q^2 dependence of $\gamma^* N \leftrightarrow \Delta$ transition form-factors. *Phys. Rev. Lett.* **83**, 4494–4497 (1999).
8. Sato, T. & Lee, T. Dynamical study of the Delta excitation in N (e, e-prime pi) reactions. *Phys. Rev. C* **63**, 055201 (2001).
9. Drechsel, D., Hanstein, O., Kamalov, S. S. & Tiator, L. A Unitary isobar model for pion photoproduction and electroproduction on the proton up to 1-GeV. *Nucl. Phys.* **A645**, 145–174 (1999).
10. Kamalov, S., Chen, G.-Y., Yang, S.-N., Drechsel, D. & Tiator, L. Pi0 photoproduction and electroproduction at threshold within a dynamical model. *Phys. Lett. B* **522**, 27–36 (2001).
11. Arndt, R. A., Briscoe, W. J., Strakovsky, I. I. & Workman, R. L. Analysis of pion photoproduction data. *Phys. Rev.* **C66**, 055213 (2002).
12. Buchmann, A. J. Electromagnetic N \rightarrow Δ transition and neutron form-factors. *Phys. Rev. Lett.* **93**, 212301 (2004).
13. Pascalutsa, V. & Vanderhaeghen, M. Large- N_c relations for the electromagnetic nucleon-to- Δ form factors. *Phys. Rev.* **D76**, 111501(R) (2007).
14. Riordan, S. *et al.* Measurements of the Electric Form Factor of the Neutron up to $Q^2=3.4 \text{ GeV}^2$ using the Reaction ${}^3\text{He}(\vec{e}, e'n)pp$. *Phys. Rev. Lett.* **105**, 262302 (2010).

15. Geis, E. *et al.* The Charge Form Factor of the Neutron at Low Momentum Transfer from the ${}^2\vec{H}(\vec{e}, e'n)p$ Reaction. *Phys. Rev. Lett.* **101**, 042501 (2008).
16. Ye, Z., Arrington, J., Hill, R. J. & Lee, G. Proton and Neutron Electromagnetic Form Factors and Uncertainties. *Phys. Lett.* **B777**, 8–15 (2018).
17. Kelly, J. J. Simple parametrization of nucleon form factors. *Phys. Rev.* **C70**, 068202 (2004).
18. Sparveris, N. F. *et al.* Investigation of the conjectured nucleon deformation at low momentum transfer. *Phys. Rev. Lett.* **94**, 022003 (2005).
19. Elsner, D. *et al.* Measurement of the LT-asymmetry in π^0 electroproduction at the energy of the $\Delta(1232)$ resonance. *Eur. Phys. J.* **A27**, 91–97 (2006).
20. Kelly, J. J. *et al.* Recoil polarization measurements for neutral pion electroproduction at $Q^2 = 1$ (GeV/c)² near the Delta resonance. *Phys. Rev.* **C75**, 025201 (2007).
21. Madey, R. *et al.* Measurements of G_E^n/G_M^n from the ${}^2H(\vec{e}, e'\vec{n})^1H$ reaction to $Q^2 = 1.45$ (GeV/c)². *Phys. Rev. Lett.* **91**, 122002 (2003).
22. Schlimme, B. S. *et al.* Measurement of the neutron electric to magnetic form factor ratio at $Q^2 = 1.58$ GeV^2 using the reaction ${}^3\vec{H}e(\vec{e}, e'n)pp$. *Phys. Rev. Lett.* **111**, 132504 (2013).
23. Glazier, D. I. *et al.* Measurement of the electric form-factor of the neutron at $Q^2 = 0.3$ (GeV/c)² to 0.8 (GeV/c)². *Eur. Phys. J.* **A24**, 101–109 (2005).
24. Plaster, B. *et al.* Measurements of the neutron electric to magnetic form-factor ratio G_{En}/G_{Mn} via the ${}^2H(\vec{e}, e', \vec{n})^1H$ reaction to $Q^2 = 1.45$ (GeV/c)². *Phys. Rev.* **C73**, 025205 (2006).
25. Zhu, H. *et al.* A Measurement of the electric form-factor of the neutron through $\vec{d}(\vec{e}, e'n)p$ at $Q^2 = 0.5$ (GeV/c)². *Phys. Rev. Lett.* **87**, 081801 (2001).
26. Warren, G. *et al.* Measurement of the electric form-factor of the neutron at $Q^2 = 0.5$ and 1.0 GeV^2/c^2 . *Phys. Rev. Lett.* **92**, 042301 (2004).
27. Rohe, D. *et al.* Measurement of the neutron electric form-factor $G_{(en)}$ at 0.67 (GeV/c)² via ${}^3\vec{H}e(\vec{e}, e'n)$. *Phys. Rev. Lett.* **83**, 4257–4260 (1999).
28. Bermuth, J. *et al.* The Neutron charge form-factor and target analyzing powers from ${}^3\vec{H}e(\vec{e}, e'n)$ scattering. *Phys. Lett.* **B564**, 199–204 (2003).
29. Eden, T. *et al.* Electric form factor of the neutron from the ${}^2\vec{H}(\vec{e}, e'n)^1H$ reaction at $Q^2=0.255$ (GeV/c)². *Phys. Rev. C* **50**, R1749–R1753 (1994).
30. Ostrick, M. *et al.* Measurement of the Neutron Electric Form Factor $G_{E,n}$ in the Quasifree ${}^2H(\vec{e}, e' \vec{n})p$ Reaction. *Phys. Rev. Lett.* **83**, 276–279 (1999).
31. Golak, J., Ziemer, G., Kamada, H., Witała, H. & Glöckle, W. Extraction of electromagnetic neutron form factors through inclusive and exclusive polarized electron scattering on a polarized ${}^3\text{He}$ target. *Phys. Rev. C* **63**, 034006 (2001).
32. Herberg, C. *et al.* Determination of the neutron electric form-factor in the $D(e, e' n)p$ reaction and the influence of nuclear binding. *Eur. Phys. J.* **A5**, 131–135 (1999).
33. Galster, S. *et al.* Elastic electron-deuteron scattering and the electric neutron form factor at four-momentum transfers $5\text{fm}^{-2} < q^2 < 14\text{fm}^{-2}$. *Nucl. Phys. B* **32**, 221–237 (1971).
34. Gentile, T. & Crawford, C. Neutron charge radius and the neutron electric form factor. *Phys. Rev. C* **83**, 055203 (2011).
35. Kopecky, S. *et al.* Neutron charge radius determined from the energy dependence of the neutron transmission of liquid Pb-208 and Bi-209. *Phys. Rev.* **C56**, 2229–2237 (1997).
36. Koester, L. *et al.* Neutron electron scattering length and electric polarizability of the neutron derived from cross-sections of bismuth and of lead and its isotopes. *Phys. Rev.* **C51**, 3363–3371 (1995).
37. Aleksandrov, Yu. A., Vrana, M., Manrique, G. J., Machekhina, T. A. & Sedlakova, L. N. Neutron rms radius and electric polarizability from data on the interaction of slow neutrons with bismuth. *Sov. J. Nucl. Phys.* **44**, 900–902 (1986).
38. Krohn, V. E. & Ringo, G. R. Reconsiderations of the electron - neutron scattering length as measured by the scattering of thermal neutrons by noble gases. *Phys. Rev.* **D8**, 1305–1307 (1973).
39. Miller, G. A. Charge Density of the Neutron and Proton . *Phys. Rev. Lett.* **99**, 112001 (2007).

40. Xiong, W. *et al.* A small proton charge radius from an electron–proton scattering experiment. *Nature* **575**, 147–150 (2019).
41. Alexandrou, C. *et al.* Proton and neutron electromagnetic form factors from lattice QCD. *Phys. Rev.* **D100**, 014509 (2019).
42. Maiani, L., Martinelli, G., Paciello, M. & Taglienti, B. Scalar Densities and Baryon Mass Differences in Lattice QCD With Wilson Fermions. *Nucl. Phys. B* **293**, 420, DOI: [10.1016/0550-3213\(87\)90078-2](https://doi.org/10.1016/0550-3213(87)90078-2) (1987).
43. Capitani, S. *et al.* The nucleon axial charge from lattice QCD with controlled errors. *Phys. Rev. D* **86**, 074502, DOI: [10.1103/PhysRevD.86.074502](https://doi.org/10.1103/PhysRevD.86.074502) (2012). [1205.0180](https://arxiv.org/abs/1205.0180).
44. Alexandrou, C. *et al.* Nucleon strange electromagnetic form factors. *Phys. Rev. D* **101**, 031501, DOI: [10.1103/PhysRevD.101.031501](https://doi.org/10.1103/PhysRevD.101.031501) (2020). [1909.10744](https://arxiv.org/abs/1909.10744).